CONCENTRATED SOLAR IN A FLUIDIZED BED

BY

ALEX TERME TURMO

DEPARTMENT OF MECHANICAL, MATERIALS AND AEROSPACE ENGINEERING

Submitted in partial fulfillment of the requirements for the degree of

Master of Engineering in Mechanical and Aerospace Engineering

in the Graduate College of the

Illinois Institute of Technology

Supervised by Dr. Hamid Arastoopour

Chicago, Illinois

08/19/2017

Content

1 Acknowledgments

I would like to express my special appreciation and thanks to my advisor Hamid Arastoopour and to Deniz Hinz and Farnaz Esmaeili for guiding me in this project and give me all their support, understanding, motivation and patience.

To all my family and friends for their unconditional faith and support.

2 List of Figures

3 List of Tables

4 List of Symbols

Symbol	Definition
A	Bed cross-sectional area of t (m^2)
A_i	Interfacial area (m^2)
C	Concentration factor
C_{DO}	Drag coefficient
C_{p_k}	Specific heat of k phase (J/K)
d_b	Bubble diameter (m)
d_p	Particle diameter (m)
g	Gravity (m/s^2)
h_k	Specific enthalpy of k phase (J/kg)
h_{kj}	Heat transfer coefficient
H_w	Bed height (m)
M_s	Mass of solids in the bed (kg)
Nu_k	Nusselt Number of k phase
Pr_k	Prandtl Number of k phase
Q_{kj}	Volumetric rate of energy transfer between phase k and j (J/ m^3)
Re_p	Particle Reynolds number
T_k	Temperature of k phase
$\vec{v}_k$	Velocity of k phase (m/s)

Greek symbols

α_k	Thermal diffusivity of k phase (m/s^2)
β	Drag coefficient
β_{kj}	Drag coefficient between k phase and j phase
ε_k	Volume fraction of k phase
ε_w	Bed voidage
κ_k	Thermal conductivity of k phase
μ_g	Viscosity of phase k (kg/m s)
ρ_f	Density of fluidizing fluid (kg/m^3)

ρ_k	Density of k phase (kg/m$^{3)}$
ρ_s	Apparent density of bed particles (kg/m^3)
τ_k	Stress tensor of k phase (Pa)
Δp_w	Bed pressure drop (Pa)

5 Abstract

The aim of this thesis is to create a CFD model of a fluidized bed to study the heat transfer having concentrated solar as a heat source. First, some background about concentrated solar energy, a review of its actual potentials and barriers and a comparison among other energy sources will be exposed. Then the fluidized bed concept and the recent studies about heat transfer will be presented and discussed.

The core of the thesis will be based in creating a CFD model to predict the behavior and understand the interactions in a fluidized bed when is irradiated with concentrated solar. It has been decided to create a 2-D model of a rectangular fluidized bed with solid particles of SiC. First, the model has been tested and validated without the heat source and then the heat source has been added. Once the simple model has shown the desired results it has been upgraded including heat to the model. A crucial part of the study was how to model the heat source and how to implement it into the model. With the data obtained from current studies an approach of the heat source to a Gaussian distribution with its peak in the focal point has been made. Then this heat source has been introduced in the model affecting always the surface of the bed.

Once the heat model has been set up two different cases have been studied: a fixed bed and a fluidized bed. In the fixed bed case, the temperature in the focal point increase very rapidly like in the current studies due to that a high amount of energy is concentrated in a very small region. On the fluidized bed case, the temperature of the bed fluctuates due to the high mixing and interaction that there is in the bed that improves the heat transfer between the solid particles.

6 Concentrated solar energy

6.1 Definition

Concentrated solar energy consists in concentrate the energy coming from the sun using mirrors or lenses into a receiver. The purpose of concentrating the energy of the sun is to obtain higher temperatures in the receiver that would yield to higher efficiencies of the system. Nowadays concentrated solar is used basically in concentrated solar power plants to produce electricity. To produce electricity, the light of the sun in concentrated into the receiver, heating up a working fluid. Normally, this working fluid exchange heat with water for generating steam. Finally, this steam runs a turbine connected to a generator to produce the electricity.

One of the main reasons why concentrated solar power is so promising is because by concentrating the light the efficiencies of concentrated solar system increase. One parameter that is important to have in mind in these type of systems is the concentration ratio (C). The concentration ratio can be defined as the ratio between the radiant flux after the concentration and before the concentration. Considering that the area of the receiver is very small compared with area of reflection we can define the concentration factor as:

$$C = \frac{aperture\ area}{absorber\ area} \qquad (3.1)$$

Where the aperture area is the area facing the sun, and the absorber area is the area where the sun beams are concentrated. In *Figure 6.1* it can be observed that as we increase the concentrated factor, the efficiency of the CSP system increase. However, we must consider that the efficiency doesn't increase linearly with the increase of temperature, so the optimal operating temperature for each system must be determined.

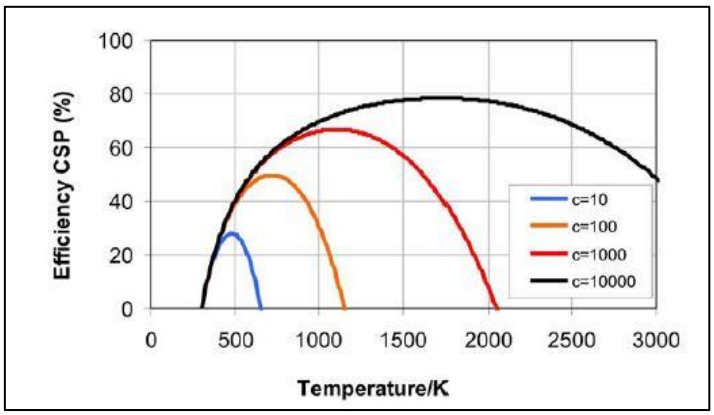

Figure 6.1 Theoretical efficiency of a CSP-system as a function of temperature for different concentration factors [12]

In *Figure 6.2* it can be shown that the temperature increase with the temperature reaching a maximum of the concentrating factor of 46200 due to optical and geometrical properties that yields to a maximum temperature in the absorber of 5780K. These two values give us the operating frame of concentrating factors and temperature that the CSP could operate.

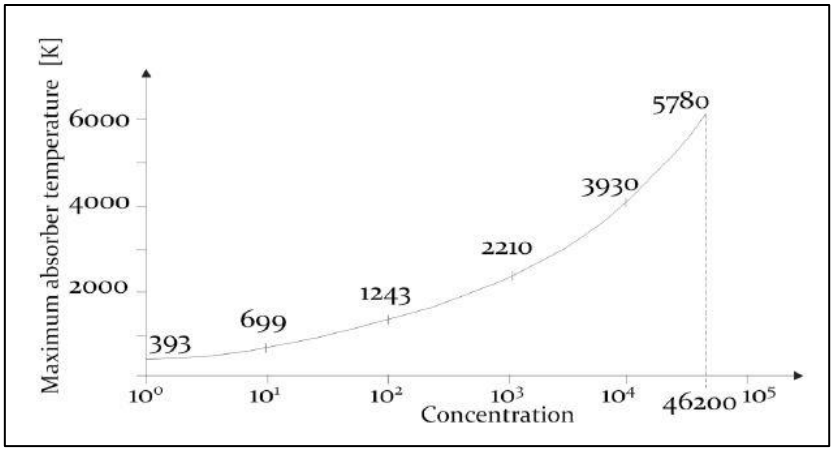

Figure 6.2 Theoretical maximum temperature at different concentration ratios [13]

6.2 Types of concentrated solar systems

There are several ways of concentrating the energy coming from the sun but all of them are based in reflecting the sun beans from a big surface into a smaller surface to achieve a high concentrator factor that would yield to higher temperatures in the receiver and higher efficiencies of the system. There are two types of concentrating systems, the ones that concentrate the sun beams in a line and the ones that concentrate it in a point. In the first category, we can find the Parabolic Trough and the Linear Fresnel. In the second category, we can distinguish between the Solar Tower and the Dish Stirling. In this section, a brief review of all of them will be provided and the main advantages and disadvantages will be discussed.

Figure 6.3.Parabolic through (up, left), Linear Fresnel (up, right), Solar Tower (bottom, left), Dish Stirling (bottom, right)

- Parabolic Through: This system uses cylindrical parabolic mirrors to concentrates the sun beams into a receiver located in the focus of the ellipse. The main parts of this system are the mirrors, the receiver and the tracking system that follows the sun during the day. This system only needs a one-axis tracking system. The operating fluid normally is oil or molten salts that can reach temperatures up to 400^{o}C. The good aspects about this technology is that is a well-known technology with high reliability but it has high construction and land requirements.
- Linear Fresnel: This system uses Fresnel lenses to concentrate the sun beams to a central pipeline. It is also a one-axis tracking system and one of the main advantages is that is composed small flat reflecting surfaces which are easier and cheaper to manufacture compared with the parabolic through. The working fluid is also oil or molten salts and the temperatures that can be reached in the receiver are similar to the parabolic trough. One of cons of this technology is that is still under development and the reliability is still unknown.
- Solar Tower: Consists of a large number of sun-tracking mirrors, called heliostats, which concentrate the sun beams into a receiver located on the top of a tower. This technology uses a two-tracking system to guarantee that all the beans are reflected to the same point. As we concentrate the energy in one point, the temperature that can be reached in the receiver is much higher than the one-axis tracking technologies and can reach values up to 1000^{o}C. This technology can use many working fluids (air, molten salts, water/steam)

- Dish Stirling: Parabolic dish shaped concentrator with a receptor in the focus. Uses a two-axis tracking system to follow the sun and the operating fluid is air. It has very high concentrator factor and the temperatures that can be reached in the receiver are up to 900ºC. One of the main advantages are its high efficiency and its modularity and its disadvantages that is still in under demonstration.

Concentration Method	line concentrating system		point concentrating system	
Technology	**Parabolic Trough**	**Linear Fresnel**	**Central Receiver**	**Parabolic Dish**
State of the Art	commercial	pre-commercial	demonstrated and first commercialisation	demonstrated
Cost of Solar Field (€/m²)	200 – 250	150 – 200	250 – 300	> 350
Typical Unit Size (MW)	5 – 200	1 – 200	10 – 100	0.010
Construction Requirements	demanding	simple	demanding	moderate
Operating Temperature	390 – 550	270 – 550	550 – 1000	800 – 900
Heat Transfer Fluid	synthetic oil, water/steam	synthetic oil, water/steam	air, molten salt, water/steam	air
Thermodynamic Power Cycle	Rankine	Rankine	Brayton, Rankine	Stirling, Brayton
Power Unit	steam turbine	steam turbine	gas turbine, steam turbine	Stirling engine
Experience	high	low	moderate	moderate
Reliability	high	unknown	moderate	high
Thermal Storage Media	molten salt, concrete, PCM	molten salt, concrete, PCM	molten salt, ceramics, PCM	molten salt, ceramics, PCM
Combination with Desalination	simple	simple	simple	Simple
Integration to the Environment	difficult	simple	moderate	Moderate
Operation requirements	demanding	simple	demanding	Simple
Land Requirement	high	low	high	Moderate

Table 6.1. LCOE of solar energy technologies at locations with high solar irradiation in 2013. Values indicate the irradiation (kWh/m^{2}a) [2]

6.3 Levelized cost of energy: Solar energy

Levelized cost of energy [1] (LCOE) is industry's primary metric for the cost of electricity produced by a generator considering all the lifetime costs. It is a figure expressed in $/kWh or $/MWh and provide the cost of generating the energy using that technology. The main costs that must be taken into consideration are: construction, financing, fuel, operation, maintenance, taxes, insurance and incentives. LCOE is a very useful tool to compare different generation options. In conventional power plants one of the most important parts of the cost is the fuel, which is very difficult to predict its price as it varies depending on the markets. In renewable energy plants, the fuel is free but the initial investment is higher compared with conventional power plants. Also, it must be considered that some countries give incentives to renewable energies which will decrease the LOCE. In Figure 6.5 can be observed the LCOE of different energy generation options. As it can be observed, solar thermal is the technology that has the highest LCOE which means that it is very expensive to produce electricity with this type of technology but more factors must be considered.

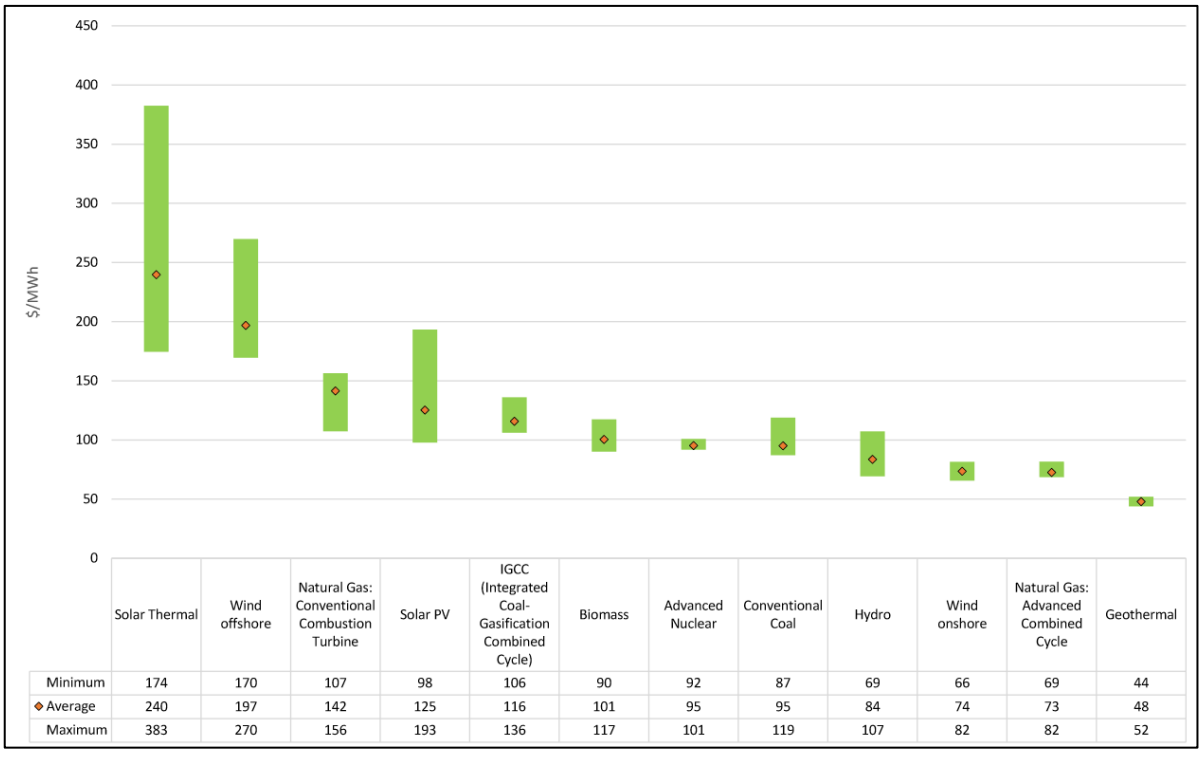

	Solar Thermal	Wind offshore	Natural Gas: Conventional Combustion Turbine	Solar PV	IGCC (Integrated Coal-Gasification Combined Cycle)	Biomass	Advanced Nuclear	Conventional Coal	Hydro	Wind onshore	Natural Gas: Advanced Combined Cycle	Geothermal
Minimum	174	170	107	98	106	90	92	87	69	66	69	44
◆ Average	240	197	142	125	116	101	95	95	84	74	73	48
Maximum	383	270	156	193	136	117	101	119	107	82	82	52

Figure 6.5. Projected LCOE in the U.S by 2020

Concentrated solar technologies will be addressed among the different types of solar thermal technologies. One of the main attractions of concentrating solar systems is its integration with thermal storage system allowing producing electricity independently

from the weather conditions. So, integrating a CSP system with a thermal storage system we can obtain a dispatchable generation with a renewable energy source. One of the main reasons why concentrated solar has slow down its evolution is because the high decrease of the price of PV panels of the last years. This fact made PV more competitive than CSP systems and made its LCOE lower compared with other solar technology. As it can be observed in Figure 6.6 the LCOE of PV is much lower, between 0.06 – 0.12 €/kWh, than the CSP technology with storage that oscillate between 0.14 – 0.19 €/kWh.

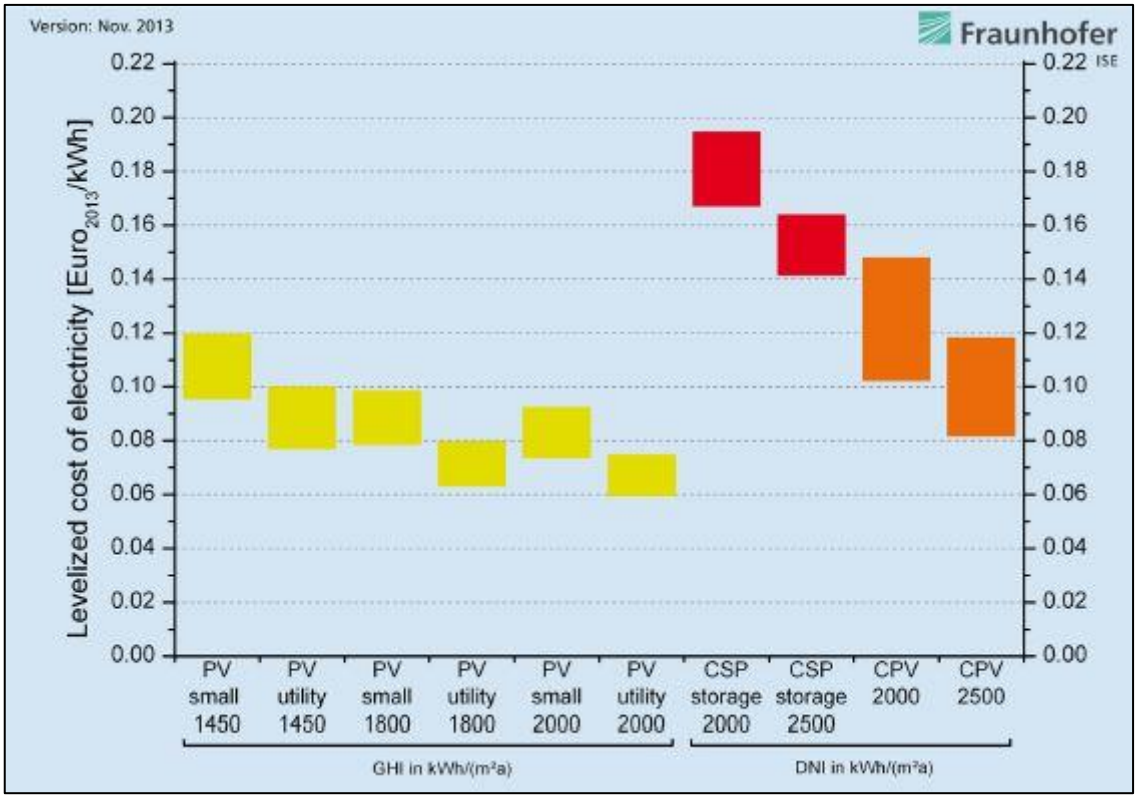

Figure 6.6. LCOE of solar energy technologies at locations with high solar irradiation in 2013. Values indicate the irradiation (kWh/m2a) [2]

Based on the study performed by Fraunhofer [2], the levelized cost of energy of CSP system varies from 0.12 to 0.25 €/kWh of plants of 100 MW. For calculating the LCOE, two irradiations have been used. The first calculation was done with an irradiation of 2000 kWh and the second one of 2500 kWh. In Figure 6.7 can be observed the LCOE of the different type of CSP technologies with and without storage with the two different annual irradiations mentioned above. It can be observed that the technology that seems to provide a lower LCOE is linear Fresnel, but some skepticism about this data must be kept. As linear Fresnel is a technology in development and only few real projects have been done there is not much data to perform an accurate LCOE calculation although with the

available data is the one has the lowest LCOE. Parabolic through with an 8-hour storage and with an irradiation of 2000 kWh/m^{2}a has a LCOE compressed between 0.161-0.197 €/kWh. It can be observed that the variability of LCOE of parabolic through systems is lower if a thermal storage is included. Finally, the most expensive theology in terms of LCOE is the solar tower. In the Fraunhofer's report the LOCE of this type of system with an 8-hour storage and with an irradiation of 2000 kWh/m^{2}a was 0.184-0.210 €/kWh. CSP technology is expected to have cost reduction due to higher automation, project experience and use of new type of materials and components. In solar tower technology, a very promising research line is the utilization of new types of receivers to maximize the heat transfer and improve the efficiency of the system.

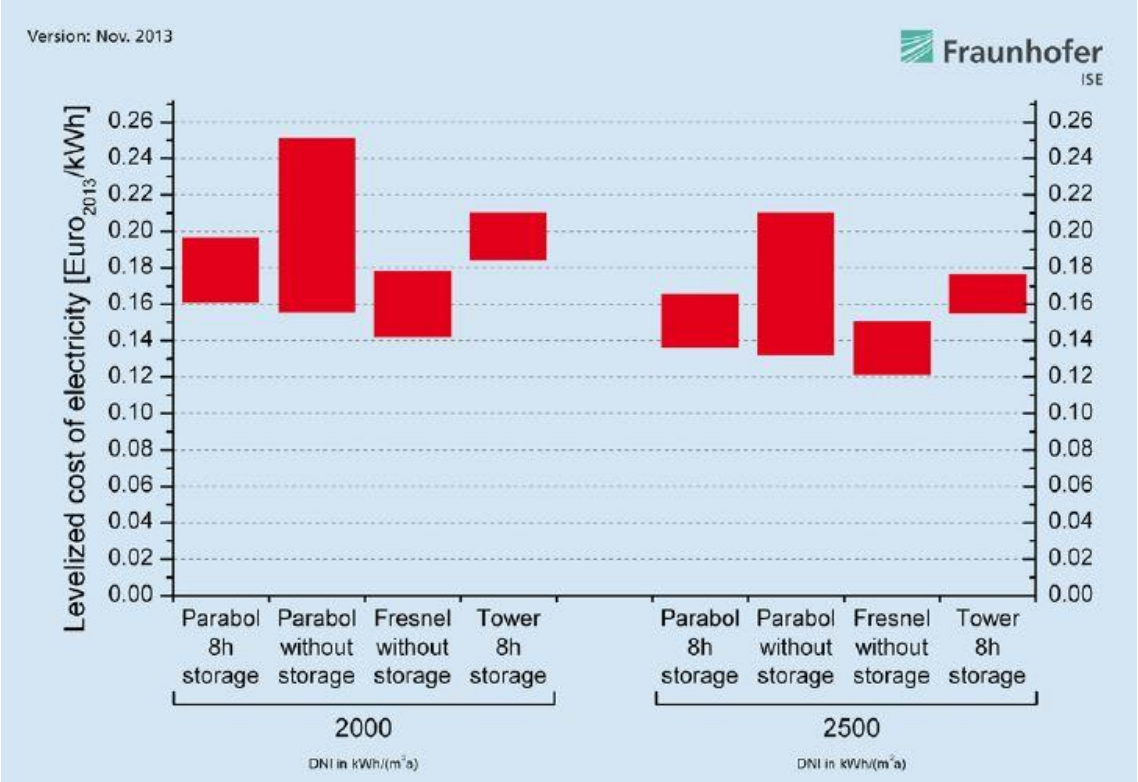

Figure 6.7. LCOE of CSP plants with nominal capacity of 100 MW, by plant type and irradiation (kWh/m^{2}a) [2]

7 Fluidized Bed technology

7.1 Introduction

A fluidized bed is a solid/fluid mixture that behaves like a fluid and it is formed when a quantity of a solid particulate substance is placed under certain conditions. A fluidized bed has many interesting properties and applications as you have solid particles that can be analyzed like a fluid. They can free-flow under gravity or to be pumped using fluid type technologies. One of the most interesting properties of a fluidized bed is that the contact between the solid particles and the fluidization medium is much greater than in conventional packed beds. This good contact between the two different phases allows a fluidized bed to have a great heat transfer between the solid particles and the fluid and between the bed and its container.

As it was commented in the previous paragraph, fluidized bed exhibit fluid properties and as it can be considered a heterogeneous mixture, a single bulk density can be used for the whole fluidized bed. As the fluidized bed can be considered as a fluid if we immerse an object with a lower density in the bed it will float to the surface. If we put an object with a higher density than the bed it will sink.

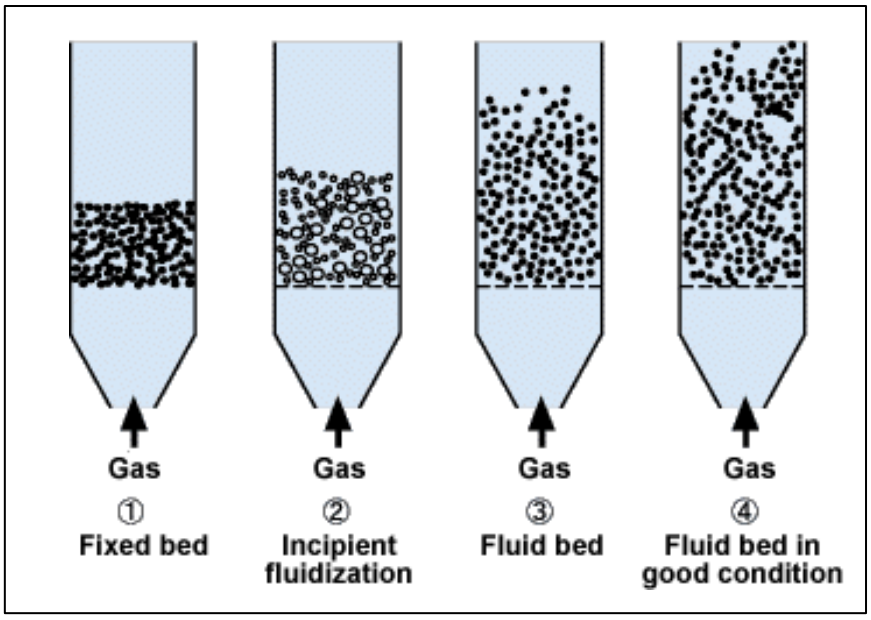

Figure 7.1. Fluidization process [16]

In *Figure 7.1*, the steps involved in the fluidization process are explained. The fluidized state occurs when a fluid at a sufficient velocity can break up the fixed bed of a particulate material. When the bed is fixed, the particles are immobile and they have numerous contact points among where contact forces are applied because of gravity. When the minimum fluidization velocity (v_{mf}) is achieved, that is the minimum velocity that the fluid must reach to be in a fluidized bed condition, the bed's mass is suspended directly by the flow of the fluid stream. In the fluidized state, the contacts between particles are of short duration and the forces between them are weak. The pressure drop across the bed is constant and directly related to the bed weight and its cross section. In *Figure 7.2* it can be observed that the pressure increase with the velocity until the v_{mf} is reached, then there is a momentary increase in the pressure and then it stabilizes at a constant pressure.

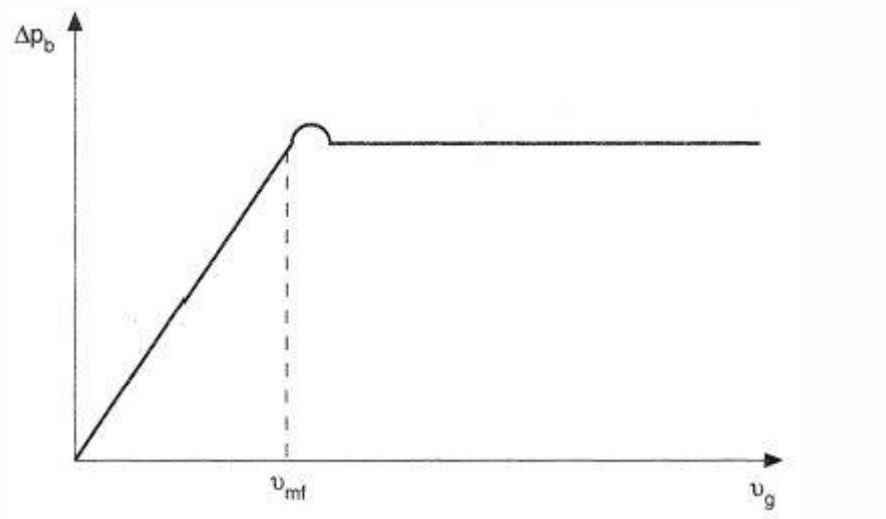

Figure 7.2 Pressure drop vs fluid velocity in a fluidized bed [15]

The pressure drop can be calculated using *equation 7.1*. It can be calculated by two different ways. The first one is knowing the bed height, the bed voidage and the apparent density of the fluidization fluid and the bed particles. The second way is using the mass of the bed, the gravity, the cross-sectional area of the bed and the apparent density of the fluidization fluid and the bed particles. This equation will be used to verify if the results obtain using the model match with the results calculated analytically.

$$\Delta p_w = H_w \cdot (1 - \varepsilon_w) \cdot (\rho_s - \rho_f) = \frac{M_s \cdot g}{A \cdot \rho_s} \cdot (\rho_s - \rho_f) \qquad (7.1)$$

When the bed is fluidized with liquids, we have the case of the "homogenous" fluidization. Gas fluidization leads to so-called "heterogeneous" fluidization. At gas velocities, just above the minimum fluidization velocity, bubbles form and the fluidized bed can be treated as if it consists of two phases: bubbles, in which there are virtually no particles and a particulate (emulsion) phase, which is in a condition like that of the bed at the minimum fluidization velocity. Bubbles which form near the distribution plate, rise the bed, grow and coalesce, producing bigger bubbles which sometimes break up into smaller bubbles. On the bed surface, bubbles eruptively burst, ejecting the particles far from the bed surface. Such bubble behavior makes particle circulation in the bed very intensive. Behind the bubble, in its trail, particles move upwards. Around the bubbles and between them, and especially near the walls, particles move downwards. Bubble movement thus promotes intensive gas and particle axial mixing in the fluidized bed.

7.2 Advantages compared with existing solutions

Nowadays concentrated solar systems tend to use molten salts or organic oils as a working fluid. These types of fluids are limited to operating temperatures up to 560^{o}C [3], they can only reach these temperatures because, for the case of nitrate salts, they decompose at temperature greater than 600^{o}C [4]. To improve the efficiency of concentrated solar systems a higher temperature is needed. In a fluidized bed receiver, solid particles are used for the heat exchange. Using the solid particles to absorb the radiation coming from the sun, temperatures greater than 1000^{o}C [5] can be achieved, which can boost the efficiency of the concentrated solar system. Moreover, using solid particles will reduce dramatically the cost of the working material. While molten salts such as Nitrate salt can cost up to 1$/kg, using solid particles such as sand or ashes, the cost can be reduced to 0.01-0.1$/kg. In actual CSP power plants, the cost of the working fluid is a significant amount of the initial investment, and must be taken into consideration that it will add high O&M cost. In Table 7.1, there is a comparison between a Nitrate Salt and a Solid Particle used as a Heat Transfer Fluid. It can be observed that using a solid particle as a HTF yields to a more efficient system, with less cost and with a lower initial investment,

including the option to add a thermal storage to the system at a very competitive price. Moreover, fluidized bed has other advantages such as: excellent gas-solid contacting, absence of hot spots even with highly exothermal reactions, good gas-to-particle and bed-to-wall heat transfer due to the intense mixture of the solid material by the presence of gas bubbles [6] Nevertheless, fluidized bed using solid particles is a very new technology and a lot of research must be done to extract is potential benefits.

Another important aspect of using a fluidized bed receiver is that higher efficiency power cycle can be used. As now the temperature it is not limited to 600ºC, the theoretical maximum thermal efficiency of the cycle (Carnot efficiency) will increase as temperatures greater then 1000ºC can be reached. With this temperature of the hot source, high efficiency cycle can be used such as combined Air-Brayton, supercritical-CO_2 Brayton and ultra-supercritical steam cycles which yields to a better performance of the thermal-to-electric conversion.

HTF / Storage Media	State-of-the-Art: Nitrate Salt ($1.00 /kg)	Our Approach: Solid Particle (e.g., ash, sand) ($0.01–0.1/kg)	Benefits of Our Approach
Precondition time	Conditioning, 3 months	None	Early revenue
Salt freezing protection	Required	None	Low O&M
Stability	<600°C	>1000°C	High efficiency
Corrosion	High with chloride impurity	No	Long life
Structure materials	Steel, stainless steel, or alloy	Ceramic/refractory/concrete	Low cost
TES cost estimation	30–75 $/kWh$_{th}$	<10 $/kWh$_{th}$	Lower LCOE
Supporting power cycles	Super-heated steam/s-CO_2	Steam-Rankine/s-CO_2/air-Brayton	Efficiency
Receiver cost estimation	Salt: ~$100s of millions	SPR, ~$10s of millions	Cost reduction
Estimated LCOE	~14¢/kWh	About 2.5¢/kWh reduction	

Table 7.1. Benchmark of the FB-CSP system to current state-of-art salt systems (100-MW$_e$ scale) [5]

7.3 Current studies

7.3.1 Heat transfer in directly irradiated fluidized bed [7]

The aim of this study was studying the heat transfer in a fluidized bed using an experimental set being able to map the bed surface temperature of the bed. Another important issue that was investigated is that when a beam of light is directly concentrated into a bed, the concentration point can reach very high temperatures that can degrade the solid particles and affect in the efficiency of the system. One possible solution to this problem is presented in the paper.

The main components that conform the experiments are:

- A fluidized bed reactor with a gas preheater and a mass flow control system.
- A temperature and pressure measurement system of the bottom bed.
- A simulated solar radiation source, consisting of a short-arc Xe lamp and of an elliptical mirror.
- An infrared camera to map the bed surface temperature.
- A Bubble Generation System (BGS) connected to a submerged nozzle located along the central axis of the fluidized bed.

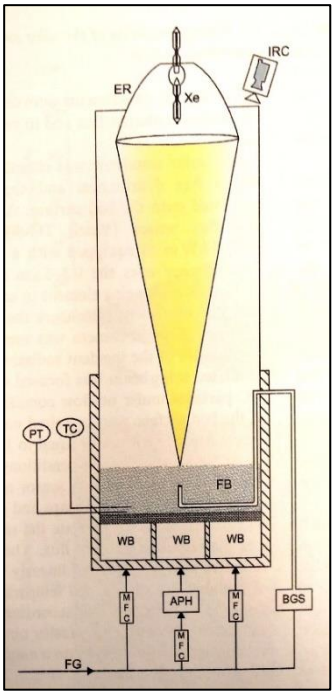

Figure 7.3. Outline of the experimental apparatus

The most important facts that can be taken advantage of that study are the way to model the sun light, the type of solid particles used and the interaction between the inlet air velocity and the surface temperature. For emulating the solar radiation, a short-arc ozone-free 4 kW_{el} was chosen. This type of lamp emits in a spectrum very similar to the spectrum emitted by the sun that reaches the Earth. The lamp is equipped with an elliptical reflector that allows to concentrate the light in a desired point. Another critical parameter for a fluidized bed is the material of the solid particles. In this study, the material was SiC powder with the physical properties shown in *Table 7.2*. That material is considered a good absorber due to its large emissivity, nearly 0.9. The emissivity is calculated using an infrared camera and a thermocouple.

Density (kg m^{-3})	Size range (µm)	Size standard deviation (µm)	Sauter mean diameter (µm)	Geldart classification group	U_{mf} ($m\ s^{-1}$)
3210	50-350	55	127	B	0.018 (20ºC) 0.016 (600 ºC)

Table 7.2. Physical properties of SiC power [7]

In that study, the temperature of the bed was measured under different operating conditions in the bed, from fixed bed to freely bubbling fluidized bed conditions. The main experiments shown are at inlet air velocities of u=0 m/s (fixed bed), u= 0.018 m/s (incipient fluidization) and u=0.073 m/s (freely fluidization). It can be observed that in a fixed bed, the temperature reached in the incident point of the bed is very higher, and can reach temperatures up to 1500ºC. For an incipient fluidization, it can be observed that a very hot spot is still formed where the light is irradiated. From the third experiment, we can conclude that when the fluidized bed is fully formed the temperature decrease dramatically down to temperatures of 150 ºC. This huge reduction in the temperature is basically due to two different factors. The first one is that bubbles promote the coverage of the hot area by the cold particles located away from the focal point. The second mechanism is that bubble busting promotes the displacement of hot particle to colder areas of the bed. It can be concluded that bubble bursting reduced local overheating in a fluidized bed. Other experiments were done using the BGS system to reduce the overheating an increase the heat transfer.

7.3.2 High-temperature fluidized receiver for concentrated solar radiation by a beam-down reflector system [8]

This study can be divided in three different parts: a numerical computation of a volumetric receiver, an experimental examination of a fluidized bed receiver and the numerical approach of that fluidized bed. Form the first part, although is not a fluidized bed, some important parameters can be studied. The volumetric receiver is formed by a porous medium of SiC, the same material used in [7]. A thermal conductivity (λ_s) of 118 W/(mK) is assumed for this specific material. In the numerical simulation, the concentrated solar light is modeled as a heat generation source of 1000 kW/m^2.

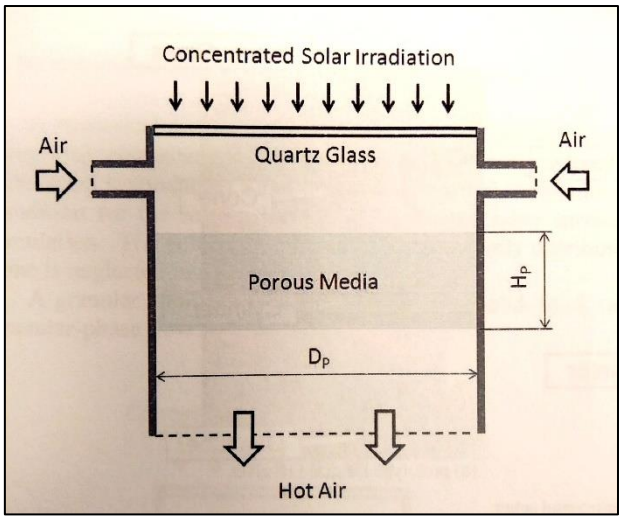

Figure 7.4. Volumetric receiver experiment

The experimental examination of the fluidized bed consists in the experiments setup shown in ***Figure 7.5***. As it can be observed air in introduced into the bed at two different velocities, the velocity of the central flow (V_D) is always 1.56 faster than the annular velocities (V_A). This fact increases the organized particle circulation. Moreover, a draft tube is submerged in the fluidized bed to stabilize its circulation. In that experiment, the material that was used to capture the concentrated light was ceramic particles of $NiFe_2O_4/mZrO_2$ with a size range of 212-710 μm. The numerical approach of that fluidized bed was done using FLUENT V.13. To treat the solid-fluid, two-phase flow a granular approach was adopted.

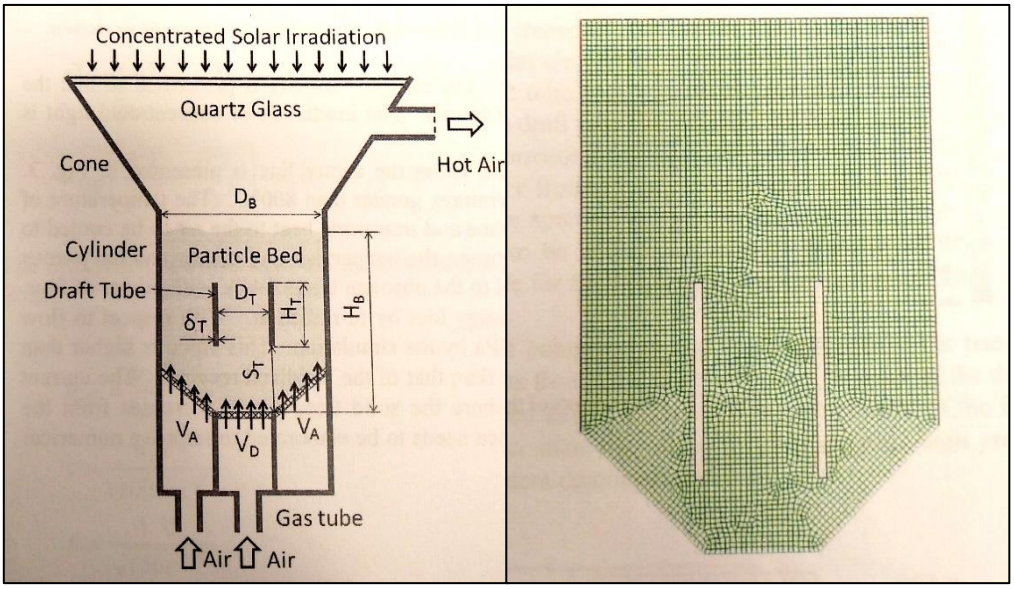

Figure 7.5. Experimental apparatus of the fluidized bed (left), Numerical approach (right)

8 Fluidized bed model

8.1 Introduction

Once the current studies have been analyzed and understood the first step will be develop a fluidized bed model. The first fluidized model will be based in the study *Heat transfer in directly irradiated fluidized bed* [7]. So, the main purpose is validating the results obtain in that study using the CFD model developed using the software FLUENT. For being able to emulate the conditions of the study first a simple model of a fluidized bed without heat transfer will be developed and tested. Once this model works correctly, a model of a fixed bed considering the heat transfer will be developed. Finally, a fluidized bed model with heat transfer will be designed. The creation of the model including the heat source is the most challenging part of this study. The main factor that must be considered is how the heat is transferred to the particles. In the experiment, the surface of the bed is directly irradiated. So, how to model this is crucial for the simulation. It must be discussed how the heat source will be, which regions of the bed will affect and how it will be implemented. To verify that the model is correct the results will be compared with the once obtain in the study [7].

8.2 Fluidized bed mathematical model [9] [10]

For this fluidized bed model, it has been decided to perform a 2-D simulation to minimize the computational time and because with a 2-D model is enough to understand the heat transfer process in the fluidized bed case studied. This model will be based in an Eulerian-Granular approach. This model uses a single pressure field for both phases, that implies that the pressure term is the same in both phases. Moreover, phases can mix and interpenetrate into one another but the volume of the phase cannot be occupied by the other phase. The volume fraction of each phase is assumed to be continuous functions and their sum is equal to one. The interaction between both phases is modeled through the following interaction terms: drag force, virtual mass effect and heat transfer coefficient.

The basic equations governing the model are the continuity, momentum and energy equations for each phase and the interaction models used in the model.

8.2.1 Conservation equations

In that section the conservation equations of mass, momentum and energy will be presented and summarized in *Table 8.1*.

The mass continuity equation both each phase is:

Gas phase:

$$\frac{\partial}{\partial t}(\varepsilon_g \rho_g) + \nabla(\varepsilon_g \rho_g \vec{v}_g) = 0 \tag{8.1}$$

Solid phase:

$$\frac{\partial}{\partial t}(\varepsilon_s \rho_s) + \nabla(\varepsilon_s \rho_s \vec{v}_s) = 0 \tag{8.2}$$

Where

$$\varepsilon_g + \varepsilon_s = 1 \tag{8.3}$$

The conservation momentum equation for each phase is:

Gas phase:

$$\frac{\partial}{\partial t}(\varepsilon_g \rho_g \vec{v}_g) + \nabla(\varepsilon_g \rho_g \vec{v}_g \vec{v}_g) = -\varepsilon_g \nabla \mathrm{P} + \nabla \cdot \tau_g + \varepsilon_g \rho_g g - \beta_{gs}(\vec{v}_g - \vec{v}_s) \tag{8.4}$$

Solid phase:

$$\frac{\partial}{\partial t}(\varepsilon_s \rho_s \vec{v}_s) + \nabla(\varepsilon_s \rho_s \vec{v}_s \vec{v}_s) = -\varepsilon_s \nabla \mathrm{P} + \nabla \cdot \tau_s + \varepsilon_s \rho_s g - \beta_{gs}(\vec{v}_s - \vec{v}_g) \tag{8.5}$$

The energy equation of each phase for the model is:

Gas phase:

$$\frac{\partial}{\partial t}(\varepsilon_g \rho_g h_g) + \nabla(\varepsilon_g \rho_g \vec{v}_g h_g) = -\varepsilon_g \frac{\partial P}{\partial t} + Q_{sg} \tag{8.6}$$

Solid phase:

$$\frac{\partial}{\partial t}(\varepsilon_s \rho_s h_s) + \nabla(\varepsilon_s \rho_s \vec{v}_s h_s) = -\varepsilon_s \frac{\partial P}{\partial t} - Q_{sg} + Q_{rad} \tag{8.7}$$

Table 8.1. Summary of conservation equations

Conservation of mass:

-Gas phase:

$$\frac{\partial}{\partial t}\left(\varepsilon_g \rho_g\right) + \nabla\left(\varepsilon_g \rho_g \vec{v}_g\right) = 0 \quad (8.1)$$

- Solid phase:

$$\frac{\partial}{\partial t}\left(\varepsilon_s \rho_s\right) + \nabla\left(\varepsilon_s \rho_s \vec{v}_s\right) = 0 \quad (8.2)$$

$$\varepsilon_g + \varepsilon_s = 1 \quad (8.3)$$

Conservation of momentum:

- Gas phase:

$$\frac{\partial}{\partial t}\left(\varepsilon_g \rho_g \vec{v}_g\right) + \nabla\left(\varepsilon_g \rho_g \vec{v}_g \vec{v}_g\right) = -\varepsilon_g \nabla \mathrm{P} + \nabla \cdot \tau_g + \varepsilon_g \rho_g g - \beta_{gs}(\vec{v}_g - \vec{v}_s) \quad (8.4)$$

- Solid phase:

$$\frac{\partial}{\partial t}\left(\varepsilon_s \rho_s \vec{v}_s\right) + \nabla\left(\varepsilon_s \rho_s \vec{v}_s \vec{v}_s\right) = -\varepsilon_s \nabla \mathrm{P} + \nabla \cdot \tau_s + \varepsilon_s \rho_s g - \beta_{gs}(\vec{v}_s - \vec{v}_g) \quad (8.5)$$

Conservation of energy:

- Gas phase:

$$\frac{\partial}{\partial t}\left(\varepsilon_g \rho_g h_g\right) + \nabla\left(\varepsilon_g \rho_g \vec{v}_g h_g\right) = -\varepsilon_g \frac{\partial P}{\partial t} + Q_{sg} \quad (8.6)$$

- Solid phase:

$$\frac{\partial}{\partial t}\left(\varepsilon_s \rho_s h_s\right) + \nabla\left(\varepsilon_s \rho_s \vec{v}_s h_s\right) = -\varepsilon_s \frac{\partial P}{\partial t} - Q_{sg} + Q_{rad} \quad (8.7)$$

8.2.2 Constitutive equations

The interaction between the solid particles and the air are modeled by the interphase exchange models that include the drag force, the heat exchange coefficient and additional lift forces. For the mathematical model presented in this section the exchange models that

have been decided to use are the Gidaspow and the Gunn for the exchange models mentioned above.

In a fluidized bed, the main interaction between the solid particles and the air are due to the drag exchange, so the model selected for the simulation must be carefully selected. It has been decided to use the Gidaspow model due to the characteristics of the simulation.

- **Drag Model**: Gidaspow

$$\beta = 150\frac{(1-\varepsilon_g)^2}{\varepsilon_g {d_p}^2} + 1.75\frac{(1-\varepsilon_g)\rho_g|v_g - v_s|}{d_p} \qquad \varepsilon_g \leq 0.8 \qquad (8.8)$$

$$\beta = \frac{3}{4}\frac{(1-\varepsilon_g)\varepsilon_g}{d_p}\rho_g|v_g - v_s|C_{DO} \qquad \varepsilon_g > 0.8 \qquad (8.9)$$

$$C_{DO} = \frac{24}{Re_p}\left[1 + 0.15Re_p^{0.687}\right] \qquad Re_p < 1000 \qquad (8.10)$$

$$C_{DO} = 0.44 \qquad Re_p < 1000 \qquad (8.11)$$

$$Re_p = \frac{\rho_g \varepsilon_g |v_g - v_s| d_p}{\mu_g} \qquad (8.12)$$

The internal energy balance for each phase is written in terms of phase enthalpy defined in Eq. 8.13. For that model, it has been decided to use the Gunn model to calculate the heat transfer coefficient. The Gunn model is applicable when the porosity range is between The Gunn model allows to calculate the Nusselt number (Nu), Eq. 8.17, needed for calculating the heat exchange coefficient (h_{kj}), Eq. 8.15. Once the heat exchange coefficient has been calculated, the volumetric transfer rate can be evaluated, Eq. 8.14.

- **Heat Exchange Coefficient**: Gunn

$$h_k = \int {C_p}_k dT_k \qquad (8.13)$$

Gas phase:

$$Q_{gs} = h_{gs}A_i(T_g - T_s) \qquad (8.14)$$

$$h_{gs} = \frac{\kappa_s Nu_g}{d_b} \qquad (8.15)$$

$$Pr_g = \frac{C_{p_g}\mu_g}{\kappa_g} \tag{8.16}$$

$$Nu_g = (7 - 10\alpha_s + 5{\alpha_s}^2)\left(1 + 0.7{Re_g}^{0.2}{Pr_s}^{1/3}\right) + (1.33 - 2.4\alpha_s + 1.2{\alpha_s}^2){Re_g}^{0.7}{Pr_g}^{1/3} \tag{8.17}$$

Solid phase:

$$Q_{sg} = h_{sg}A_i(T_s - T_g) \tag{8.18}$$

$$h_{sg} = \frac{\kappa_g Nu_s}{d_b} \tag{8.19}$$

$$Pr_s = \frac{C_{p_s}\mu_s}{\kappa_s} \tag{8.20}$$

$$Nu_s = \left(7 - 10\alpha_g + 5{\alpha_g}^2\right)\left(1 + 0.7{Re_s}^{0.2}{Pr_g}^{1/3}\right) + \left(1.33 - 2.4\alpha_g + 1.2{\alpha_g}^2\right){Re_s}^{0.7}{Pr_s}^{1/3} \tag{8.21}$$

- **Stress Tensors**

- Gas Phase:

$$\tau_g = \varepsilon_g\mu_g\left[\nabla\vec{v}_g + \left(\nabla\vec{v}_g\right)^T\right] - \frac{2}{3}\varepsilon_g\mu_g\left(\nabla\vec{v}_g\right)I \tag{8.22}$$

- Solid Phase:

$$\tau_s = \varepsilon_s\mu_s[\nabla\vec{v}_s + (\nabla\vec{v}_s)^T] - \frac{2}{3}\varepsilon_s\mu_s(\nabla\vec{v}_s)I \tag{8.23}$$

- **Stress Tensors**

- Gas Phase:

$$\tau_g = \varepsilon_g\mu_g\left[\nabla\vec{v}_g + \left(\nabla\vec{v}_g\right)^T\right] - \frac{2}{3}\varepsilon_g\mu_g\left(\nabla\vec{v}_g\right)I \tag{8.22}$$

- Solid Phase:

$$\tau_s = \varepsilon_s\mu_s[\nabla\vec{v}_s + (\nabla\vec{v}_s)^T] - \frac{2}{3}\varepsilon_s\mu_s(\nabla\vec{v}_s)I \tag{8.23}$$

Table 8.2. Summary of constitutive equations

Drag model: Gidaspow

$$\beta = 150\frac{(1-\varepsilon_g)^2}{\varepsilon_g {d_p}^2} + 1.75\frac{(1-\varepsilon_g)\rho_g|v_g - v_s|}{d_p} \qquad \varepsilon_g \leq 0.8 \qquad (8.8)$$

$$\beta = \frac{3}{4}\frac{(1-\varepsilon_g)\varepsilon_g}{d_p}\rho_g|v_g - v_s|C_{DO} \qquad \varepsilon_g > 0.8 \qquad (8.9)$$

$$C_{DO} = \frac{24}{Re_p}\left[1 + 0.15Re_p^{0.687}\right] \qquad Re_p < 1000 \qquad (8.10)$$

$$C_{DO} = 0.44 \qquad Re_p < 1000 \qquad (8.11)$$

$$Re_p = \frac{\rho_g \varepsilon_g |v_g - v_s| d_p}{\mu_g} \qquad (8.12)$$

Heat Exchange C: Gunn

$$h_k = \int C_{p_k} dT_k \qquad (8.13)$$

Gas phase:

$$Q_{gs} = h_{gs} A_i (T_g - T_s) \qquad (8.14)$$

$$h_{gs} = \frac{\kappa_s Nu_g}{d_b} \qquad (8.15)$$

$$Pr_g = \frac{C_{p_g}\mu_g}{\kappa_g} \qquad (8.16)$$

$$Nu_s = \left(7 - 10\alpha_g + 5{\alpha_g}^2\right)\left(1 + 0.7{Re_s}^{0.2}{Pr_g}^{1/3}\right) + \left(1.33 - 2.4\alpha_g + 1.2{\alpha_g}^2\right){Re_s}^{0.7}{Pr_s}^{1/3} \qquad (8.17)$$

Solid phase:

$$Q_{sg} = h_{sg} A_i (T_s - T_g) \qquad (8.18)$$

$$h_{sg} = \frac{\kappa_g Nu_s}{d_b} \qquad (8.19)$$

$$Pr_s = \frac{C_{p_s}\mu_s}{\kappa_s} \qquad (8.20)$$

$$Nu_s = \left(7 - 10\alpha_g + 5{\alpha_g}^2\right)\left(1 + 0.7{Re_s}^{0.2}{Pr_g}^{1/3}\right) + \left(1.33 - 2.4\alpha_g + 1.2{\alpha_g}^2\right){Re_s}^{0.7}{Pr_s}^{1/3} \qquad (8.21)$$

9 Cold fluidized bed case

To begin with, a fluidized bed model with no heat transfer will be created. As this is the first model all the steps will be detailed explain for a better understanding how the software operates and which are the inputs and parameters that are need for running a simulation. For developing the CFD model the following steps should be followed:

- Creating the geometry of the model.
- Mesh the geometry.
- Set up the software to perform the simulation.
- Analyzing the results and obtaining conclusions.

9.1.1 Geometry of the model and meshing

A simple design of the fluidized bed was created for the first case that was simulated. A 2-D model for the bed was created using the Ansys Fluent geometry software. The fluidized bed was modeled as a rectangle of 0.78 m width and 0.6 m height. This are the actual dimensions of the bed in the case. Once the geometry has been created, the meshing process stars. It has been decided for this fist model to have a mesh of 10000 elements. For creating the mesh, the Ansys meshing tool has been used. It has been specified the number of divisions of each edge (100 divisions), the size function (uniform), and the behavior (hard). With these parameters, a uniform rectangular mesh has been obtained So each element of the mesh has a size of 0.0078 m by 0.006 m or what is the same 7800 µm by 6000 µm. As the average particle size is 127 µm, the give a ratio mesh division by solid particle around 60. In *Figure 9.1* it can be observed the geometry model and the mesh. Moreover, the inlet, outlet and walls region have been created to set the boundary conditions in the Fluent case.

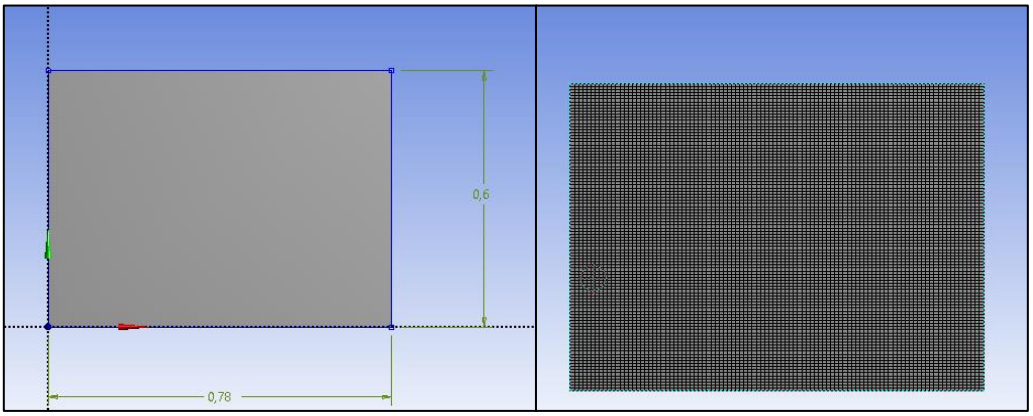

Figure 9.1. Geometry model of the fluidized bed (left), Mesh of the fluidized bed (right)

9.1.2 Set up of the simulation

In this section, all the steps that must be done to perform a Ansys Fluent simulation will be explained. As is the first simulation the parameters and assumptions will be discussed. In future simulations, only the inputs and boundary conditions will be presented so more time can be devoted to discussing and analyze the results. Although in this first simulation there is no heat transfer, the energy equation has been included in the model for using in the next simulations. Now the steps followed will be presented.

1. **Import the mesh**: First, we must import the fluidized bed mesh and check that the mesh is correct. The mesh is correct if the minimum volume is positive

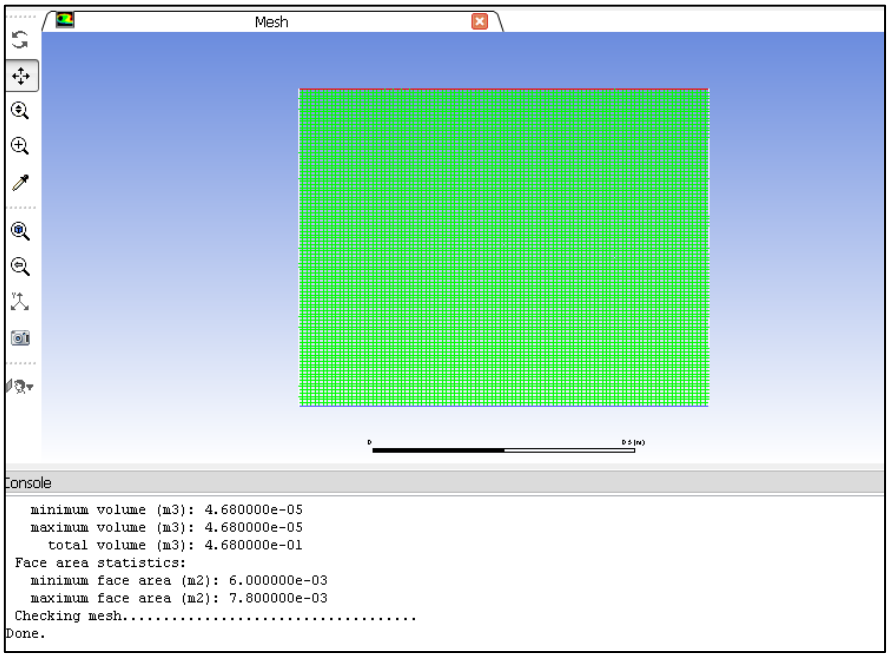

Figure 9.2. Imported mesh

2. **Solver Settings**: The type of solver, velocity formulation, time and 2D space are defined in this section. In the current simulation, the parameters selected are pressure-based, absolute, transient and planar respectively for the parameters explain above. The pressure-based solver must be used in multiphase simulation. Also, the gravity has been activated.

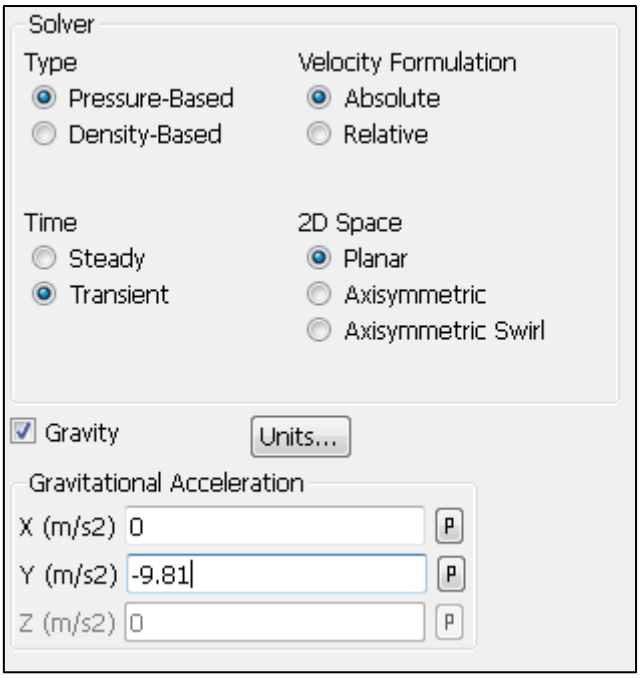

Figure 9.3. Solver and gravity settings

3. **Models**: The models used in the simulation is the Eulerian multiphase model, a laminar viscous model and the energy equation is activated.

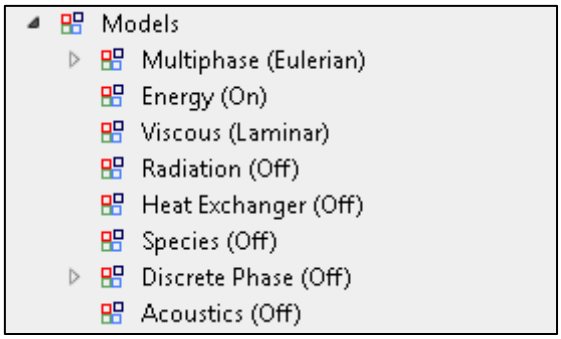

Figure 9.4. Models used in the simulation

4. **Materials**: In this model, we have two different materials: the air and the SiC particles. The properties of the materials must be defined in the software to perform the simulation. For the air phase, the default values have been selected and for the solid particles it has been created a new material with the default properties of the silicon carbide included in Fluent but modifying the density. For the silicon carbide particles, the density has been changed to 3210 kg/m^3 as is the value reported in the paper. The other properties have not specified in that simulation. It is also important to remark that the material type of the particles is fluid as we are modeling that the particle behave like a fluid. The fluidized bed

column is made of stainless steel (AISI 304) with a density of 8030 kg/m^3, a specific heat of 502.48 J/(kg-K) and a thermal conductivity of 16.27 W/(m-K) [11].

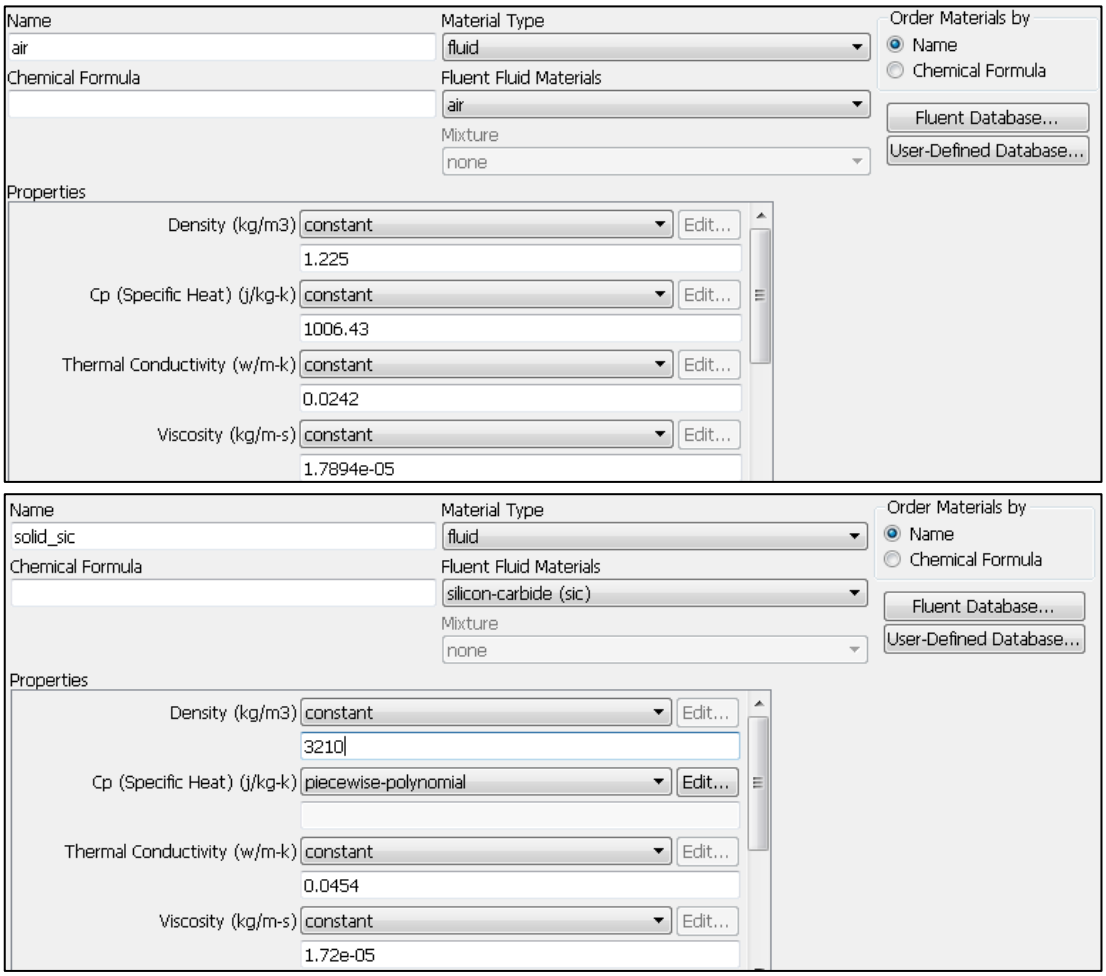

Figure 9.5. Properties of air and silicon carbide particles

5. **Phases**: The air has been defined as the primary phase and the solid as the secondary phase. At this point it has been specified that the model is granular and that for the granular temperature model it will be used the partial differential equation. The properties of the phases have been defined: Diameter (127e-6 m), Granular viscosity (syamlal-obrien), Granular Bulk Viscosity (lun-et-al), Frictional Viscosity (schaffer), Angle Of Internal Friction (30.0007 deg), Frictional Pressure (johnson-et-al), Frictional Modulus (derived), Fraction Packing limit (0.5), Granular Conductivity (syamlal-obrien), Solid Pressure (lun-

et-al), Radial Distribution (lun-et-al), Elastic Modulus (derived) and Packing limit (0.64).

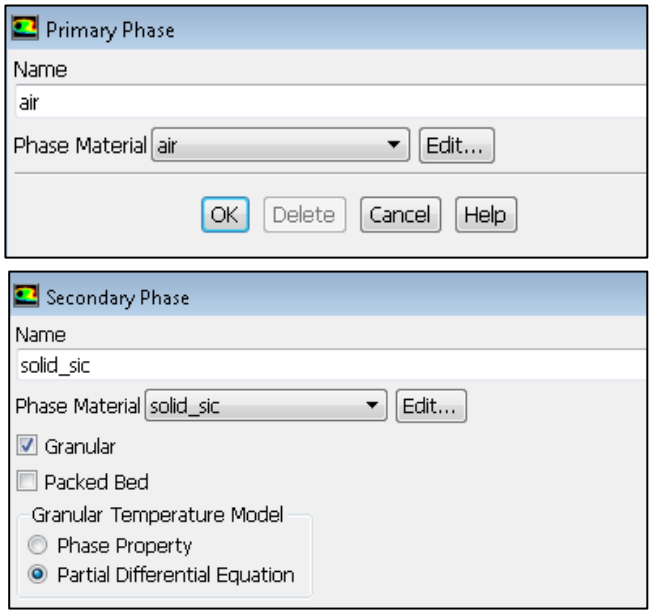

Figure 9.6. Phase designation and properties of the phase selection

6. **Phase Interaction:** In this case the phase interaction models specified are the drag coefficient and the heat transfer coefficient. For the drag coefficient, the model selected has been Gidaspow and for the heat transfer coefficient the model has been Gunn.

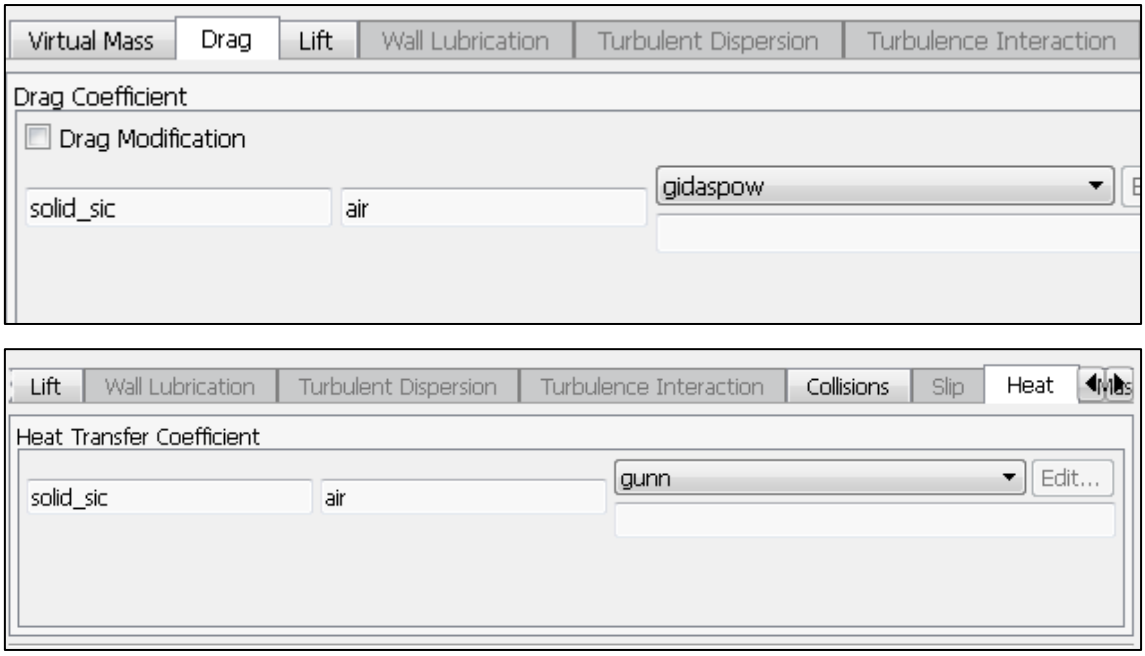

Figure 9.7. Drag and heat transfer coefficient

7. **Boundary Conditions:** For this problem, the boundary conditions must be set for the four boundaries. The four boundaries in this problem are the inlet, the outlet, the left wall and the right wall. For the Eulerian multiphase model, the inlet velocity must be specified for the primary and secondary phase. The air inlet velocity has been set as four times the minimum fluidization velocity that corresponds to 0.073 m/s. With this velocity, it can be assured that the bed will fluidized. The initial solid velocity is 0 as the bed is fixed at initial conditions. For the secondary phase the granular temperature, the volume fraction and the temperature must be also provided, these variables have been set to 0.0001, 0.55 and 298 respectively. For the two walls, a no slip condition has been applied the air phase and a specularity coefficient to the solid phase. In that first simulation, the specularity coefficient has been set to 0.9, this is an appropriate value considering the case analyzed. The granular conditions are ruled by the Johnson-Jackson equation with a restitution coefficient of 0.7. For the Eulerian model, the pressure of both phases and the mixture must be specified at the outlet boundary. For the mixture, the gauge pressure has been set to 10,000 Pa, so it is above the atmospheric pressure. For the air, the backflow total temperature has been set to 298 K. For the solid phase, the backflow temperature, the backflow granular phase and the backflow volume fraction have been specified and set to 298, 0.0001 and 0 respectively.

- **Boundary Inlet Conditions**

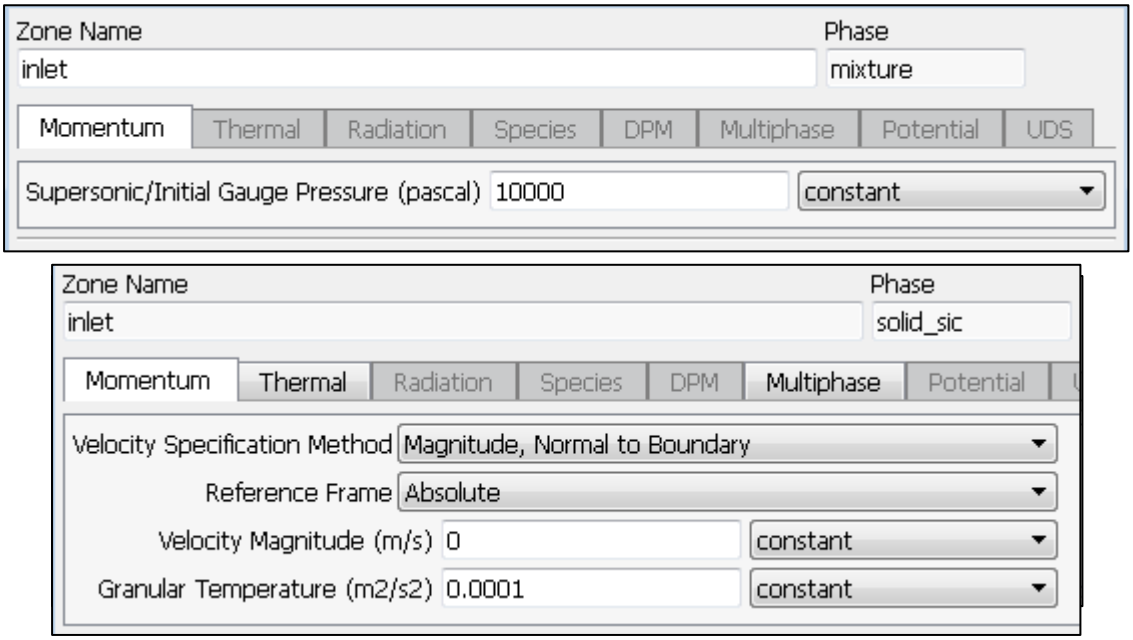

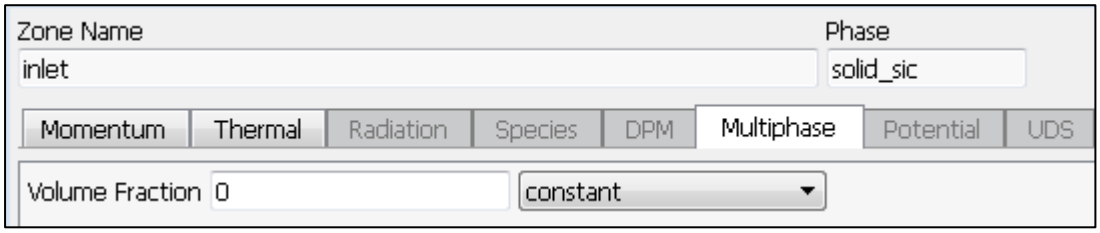

Figure 9.8. Boundary inlet conditions for the air, solid and mixture

- **Boundary wall conditions**

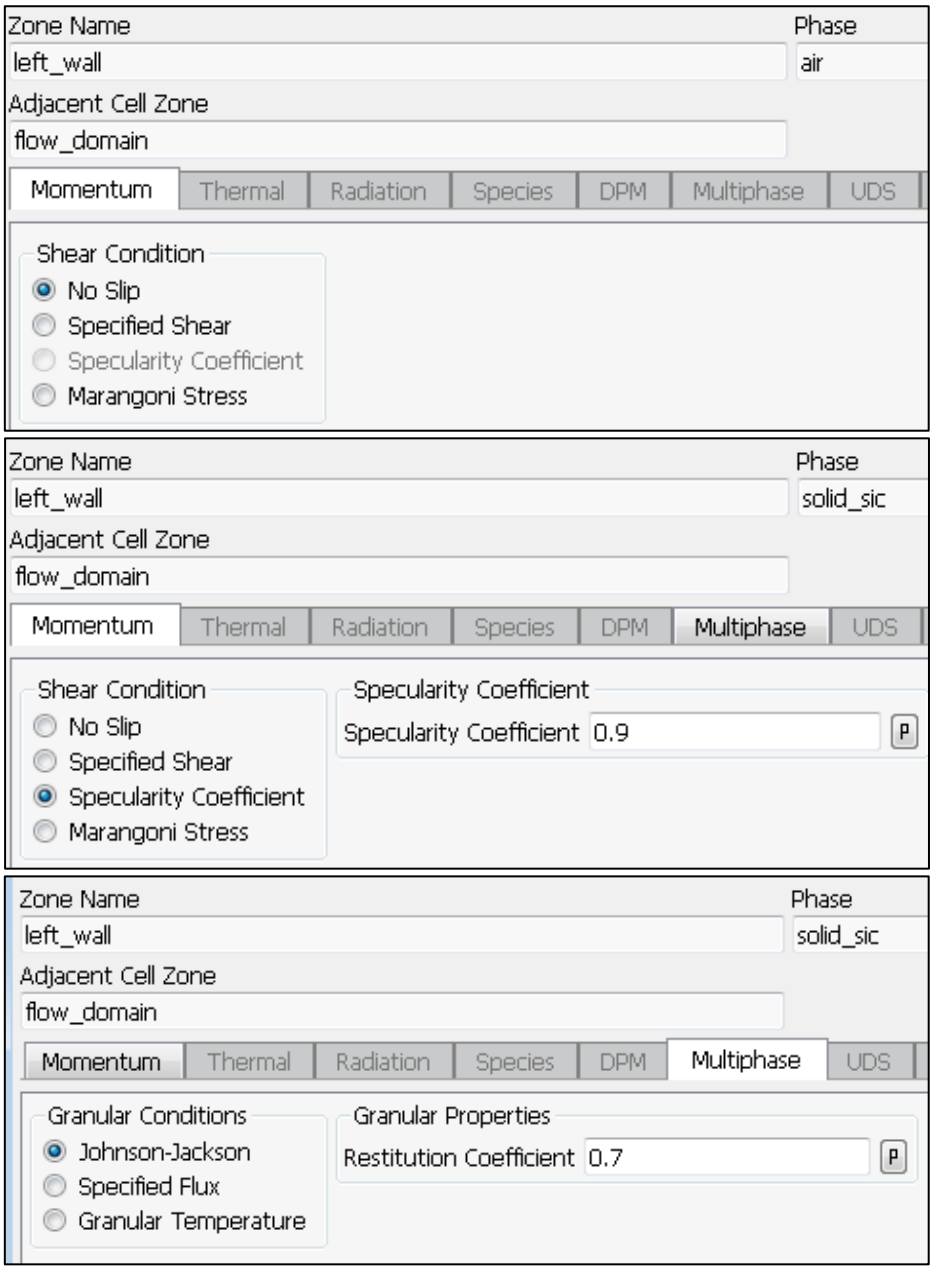

Figure 9.9. Boundary wall conditions of air and solid particles

- **Boundary outlet conditions**

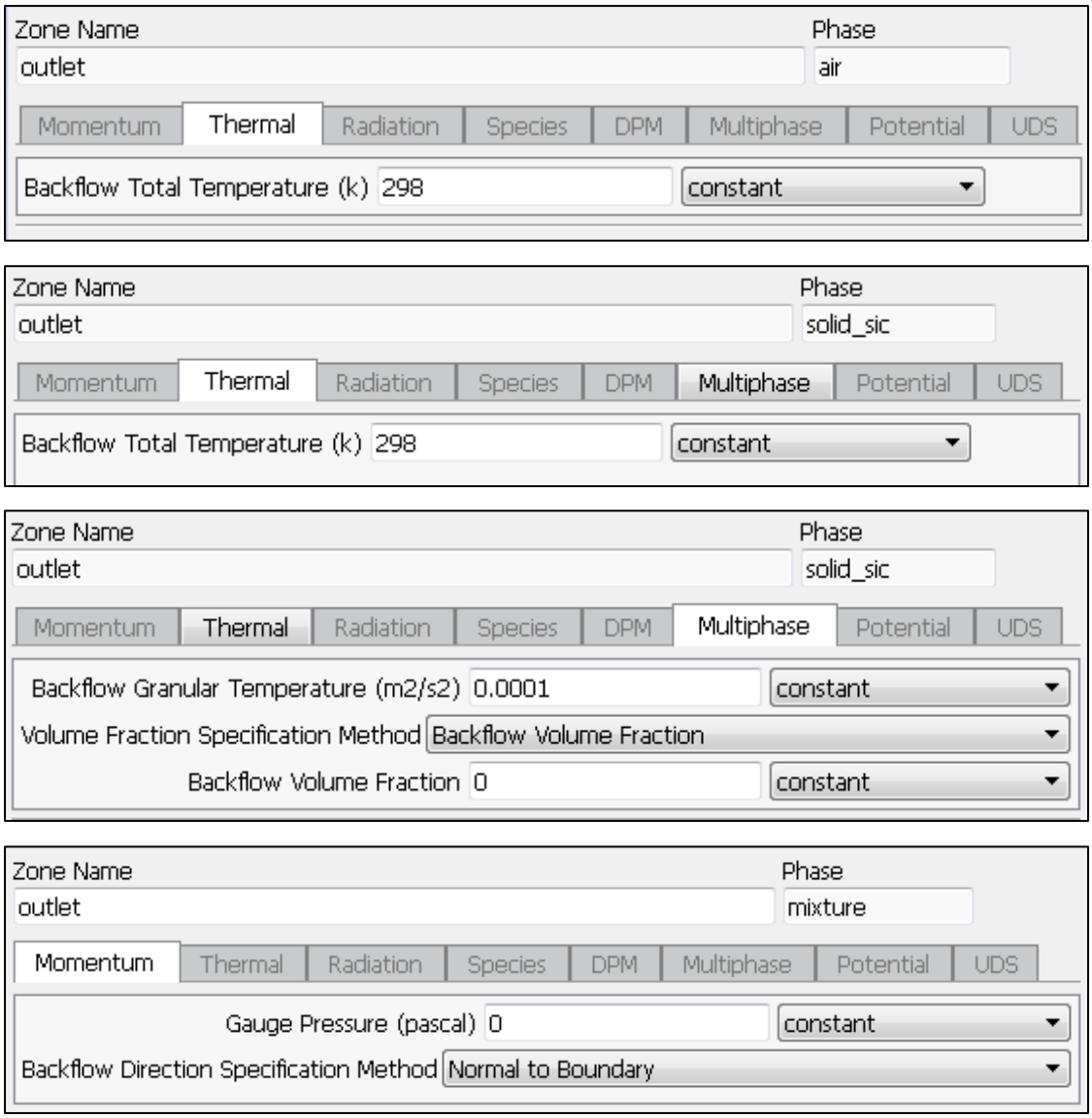

Figure 9.10. Boundary outlet conditions of air, solid particles and mixture

8. **Solution:** In that section, it must be selected the type of pressure-velocity coupling, the spatial discretization and the transient formulation that will be used to solve the problem. In the first case, we will use a Phase Coupled SIMPLE scheme, a Second Order Upwind spatial discretization and Second Order Implicit transient formulation.

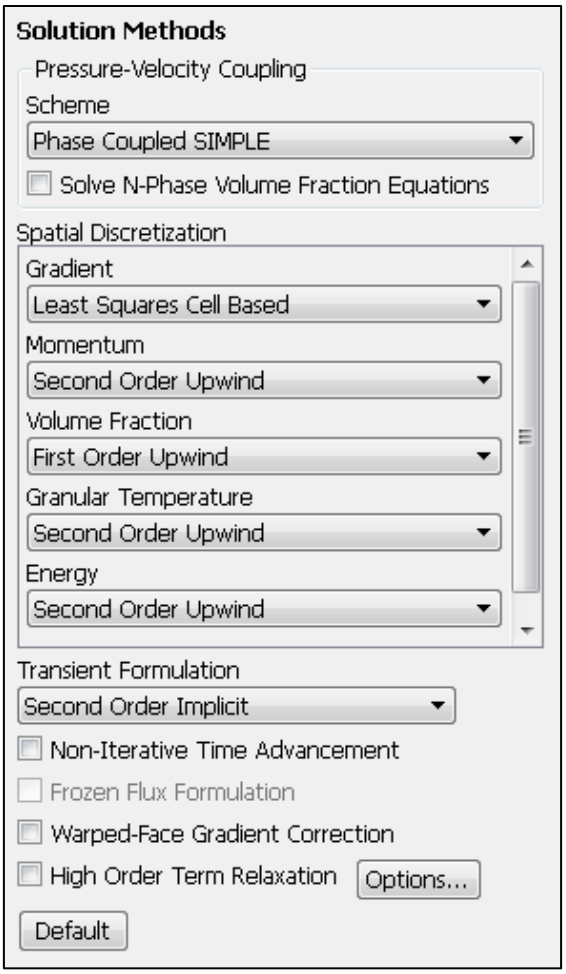

Figure 9.11. Solution methods settings

9. **Patch:** The initial volume fraction of solid in the lower part of the fluidized bed was patched with a total height of 0.2m and a volume fraction of 0.55. These are the initial conditions in the case.

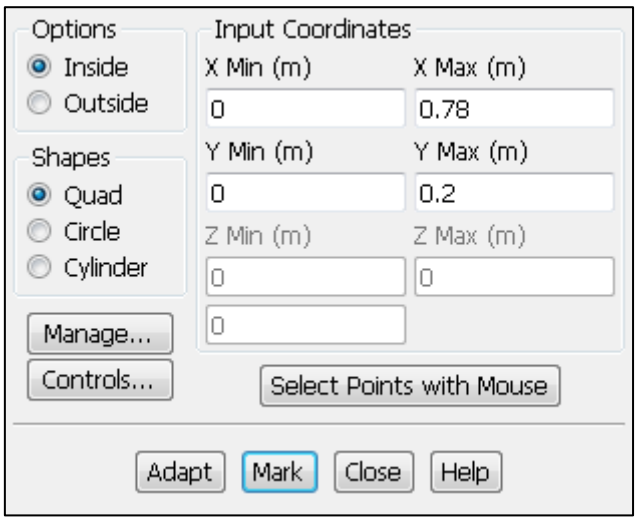

Figure 9.12. Coordinates of the geometry patched.

10. **Run calculation:** Determine how long is going to last the simulation, determine the time step size and the number of time steps and the maximum number of iterations per time step. In the first case, it has been decided to use 0.0001 seconds' time steps, a total number of 60000 times steps and a maximum of 50 iterations per time steps.

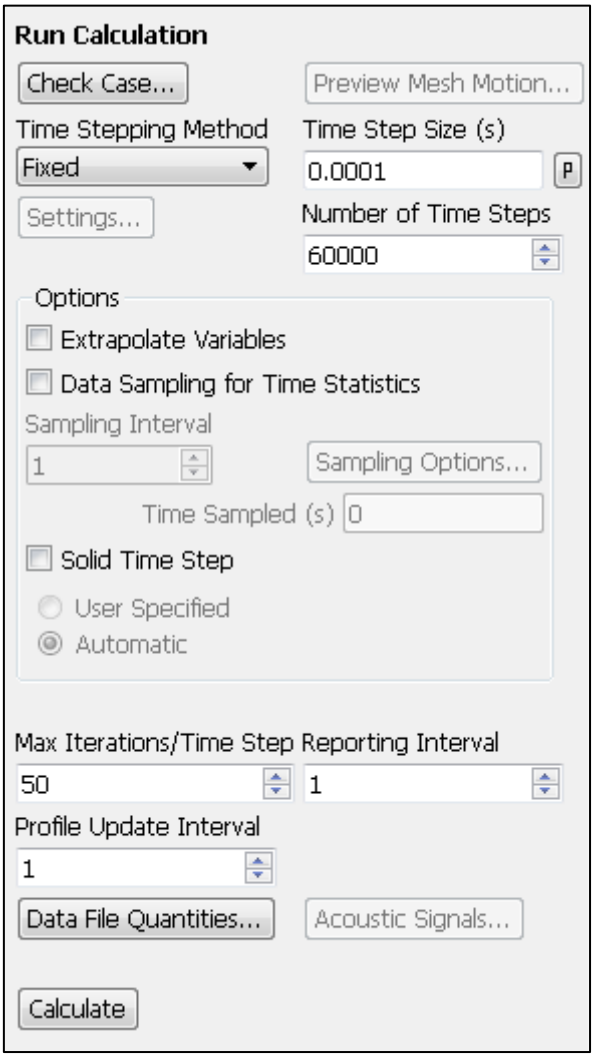

Figure 9.13. Simulation settings

The *Table 9.1* below include all the parameters that have been included to perform the simulation.

Type of Solver	Pressure-Based
Solver Velocity Function	Absolute
Solver Time	Transient
Solver 2D Space	Planar
Gravity (m/s^2)	-9.81 (Y-direction)
Multiphase Model	Eulerian
Energy Model	ON
Viscous Model	Laminar
Properties of solid phase	
Density (kg/m^3)	3210
Specific Heat (J/kg·K)	690
Thermal Conductivity (W/m·K)	118
Diameter (m)	0.000127
Granular viscosity (kg/m·s)	syamlal-obrien
Granular Bulk Viscosity (kg/m·s)	lun-et-al
Frictional Viscosity (kg/m·s)	schaffer
Angle Of Internal Friction (deg)	30.0007
Frictional Pressure (Pa)	johnson-et-al
Frictional Modulus (Pa)	derived
Fraction Packing limit	0.5
Granular Conductivity (kg/m·s)	syamlal-obrien
Solid Pressure (Pa)	lun-et-al
Radial Distribution	lun-et-al
Elastic Modulus (Pa)	derived
Packing limit	0.64
Properties of wall material	
Density (kg/m^3)	8030
Specific Heat (J/kg·K)	502.48
Thermal Conductivity (W/m·K)	16.27
Phase Interaction	
Drag Coefficient	gidaspow
Heat Transfer Coefficient	gunn
Boundary Conditions	
Air Inlet velocity (m/s)	0.073
Solid Inlet velocity (m/s)	0
Granular Temperature (m^2/s^2)	0.0001
Volume Fraction	0
Temperature (K)	298
Gauge Pressure (Pa)	10000

Air Shear Condition	No slip
Solid Shear Condition	Specularity Coefficient = 0.7
Granular Conditions	Johnson-Jackson
Restitution Coefficient	0.9
Air Back Flow Temperature (K)	298
Solid Back Flow Temperature (K)	298

Table 9.1. Input data to perform the simulation

9.1.3 Initial conditions

The simulation starts with a packed bed of 0.2 m and a solid volume fraction of 0.55. Air at four times minimum fluidization velocity (v=0.073 m/s) is being injected from the bottom of the bed. In *Figure 9.14*, it can be observed the initial solid volume fraction of the bed and in *Figure 9.15* the mixture total pressure.

- Solid Volume Fraction

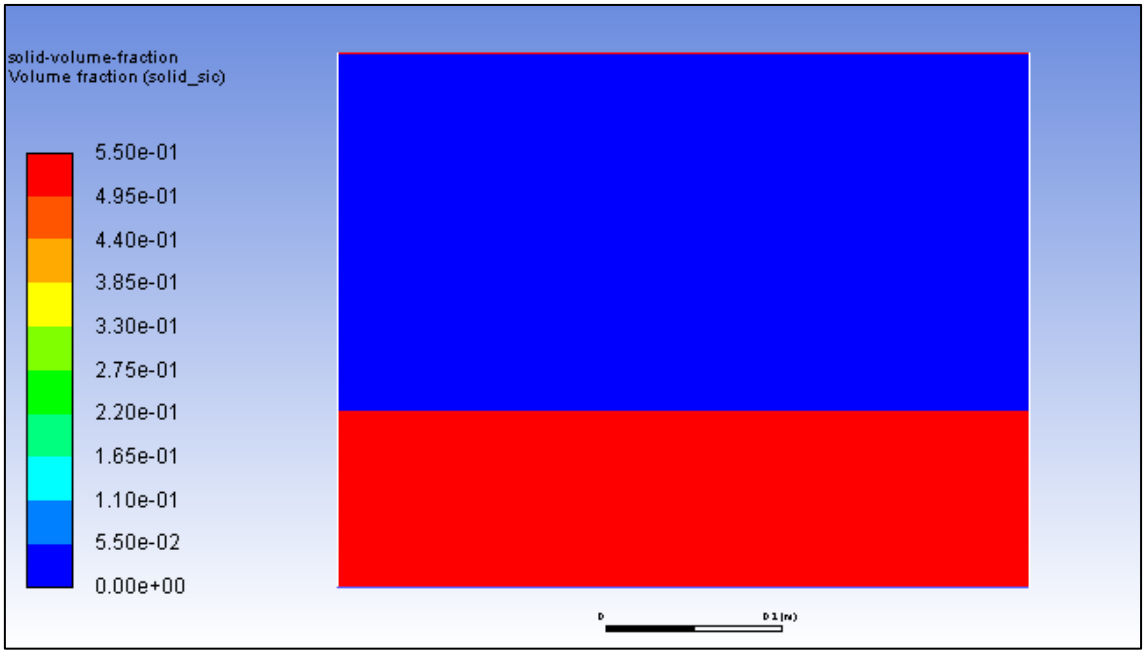

Figure 9.14 Initial solid volume fraction

- Mixture Total Pressure

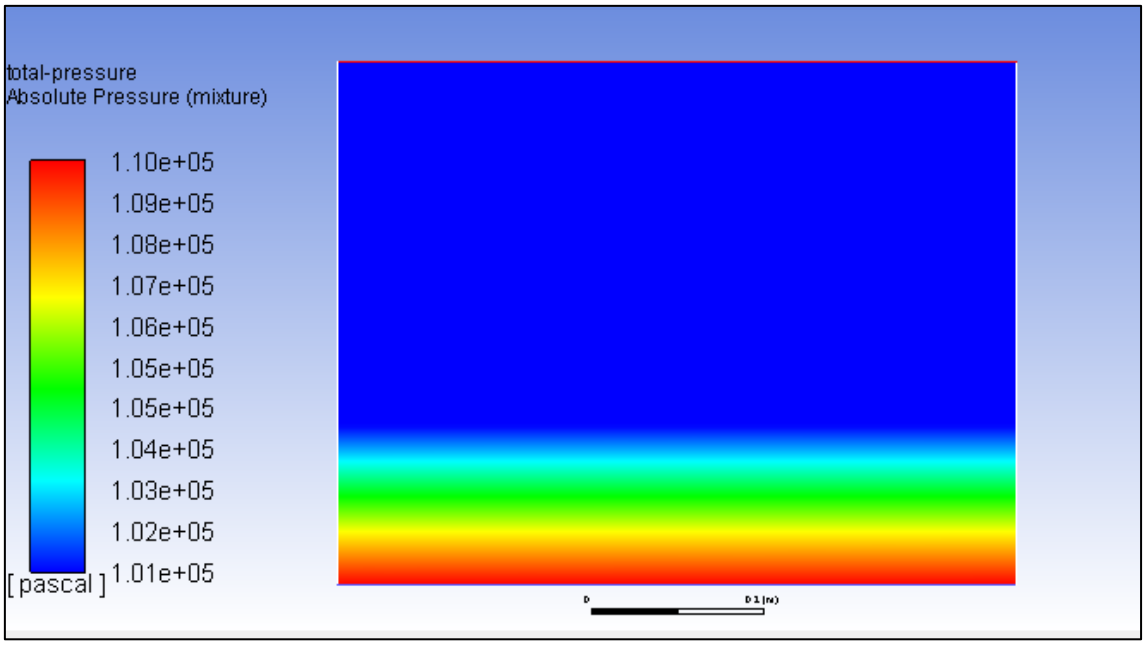

Figure 9.15. Initial mixture absolute total pressure

9.1.4 Results

The results commented in this section are from 6 second from the beginning of the simulation. With that time, it can be ensured that the air has had enough time to go through the bed and that the bed is fluidized. In *Figure 9.16*, it can be observed that the bed has risen and that the maximum solid volume has decreased to 0.513. These results were expected as the inlet temperature is above minimum fluidization.

In *Figure 9.19*, it can be observed the velocity magnitude of air. In some regions of the bed, the air speeds up to 0.402 m/s and in some of them keeps trapped at 0 velocity. These is due to the fact of the chaotic movement of the particles inside the bed. If a deeper look to the velocity components (*Figure 9.20*) is made can be noticed that the air changes direction and flows backwards in some regions of the bed, mainly in the top of the bed where the bubbles are being created.

From the solid velocity, the most interesting facto to analyze is the Y-velocity (*Figure 9.22*). Streams of solid going up and streams of solid going down are created. That makes the bed circulate and will help in the heat transfer among the different parts of the bed.

9.1.4.1 Volume Fraction

- Solid volume fraction

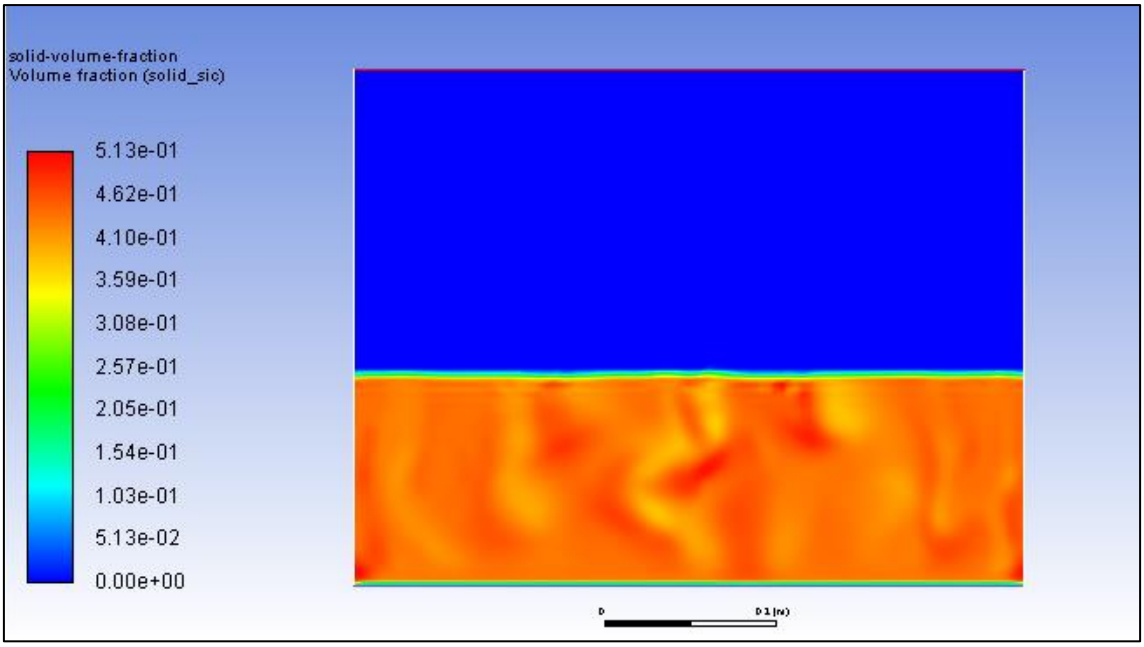

Figure 9.16. Solid volume fraction at 6s

- Air volume fraction

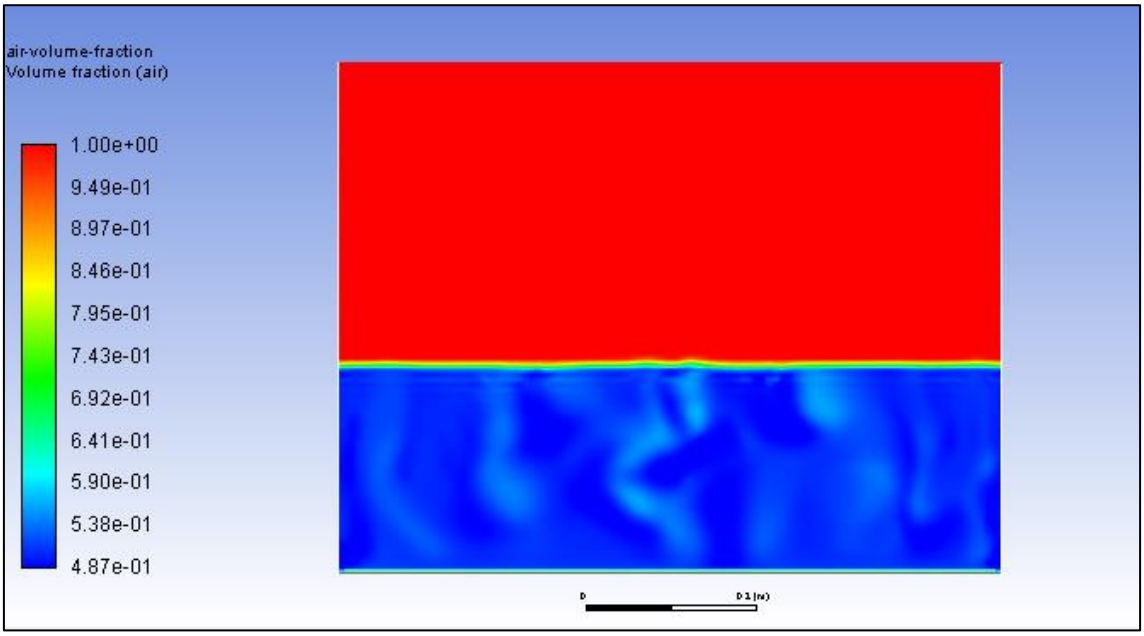

Figure 9.17. Air volume fraction at 6s

9.1.4.2 Pressure

- Mixture Absolute pressure

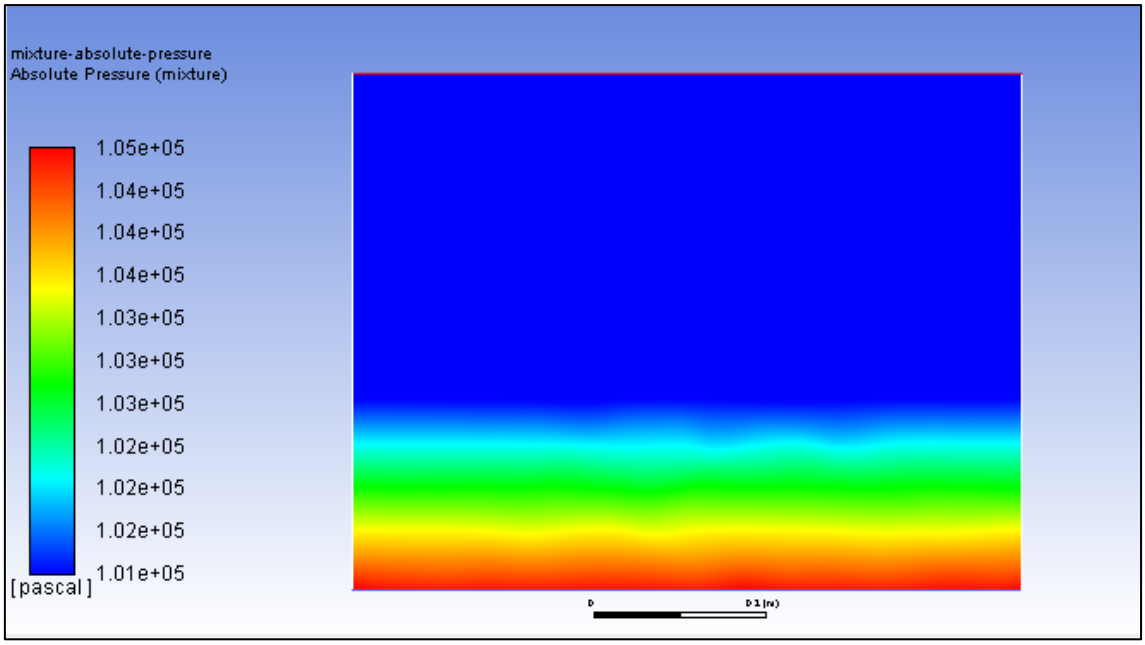

Figure 9.18. Mixture absolute pressure at 6s

9.1.4.3 Velocity

- Air velocity

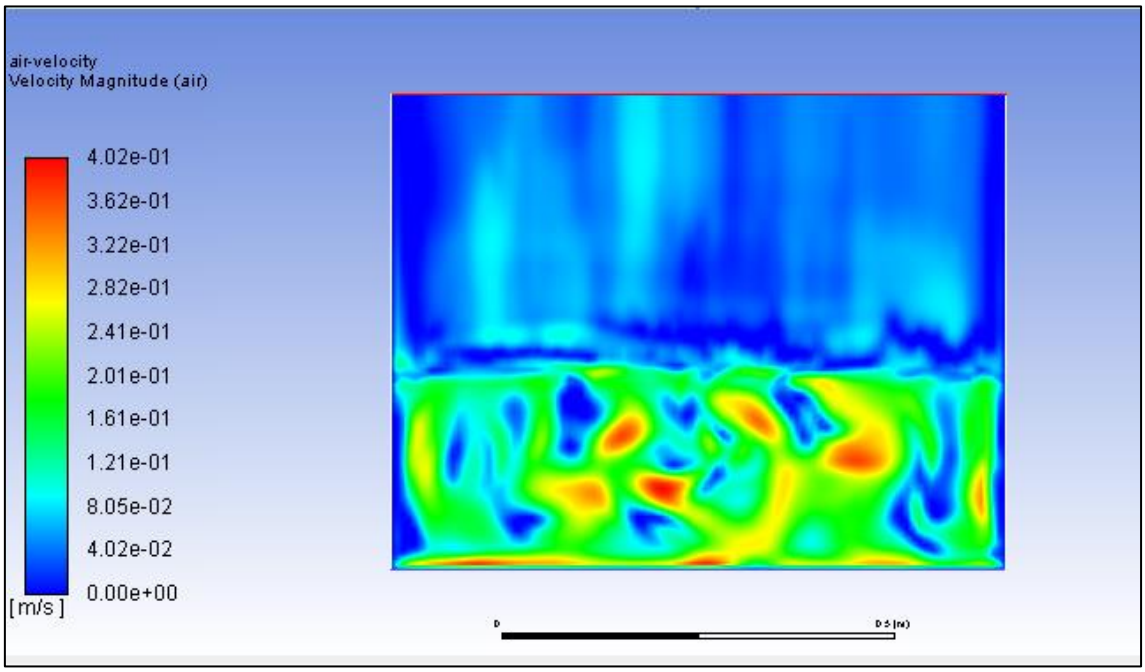

Figure 9.19. Air velocity at 6s

- Air Y-velocity

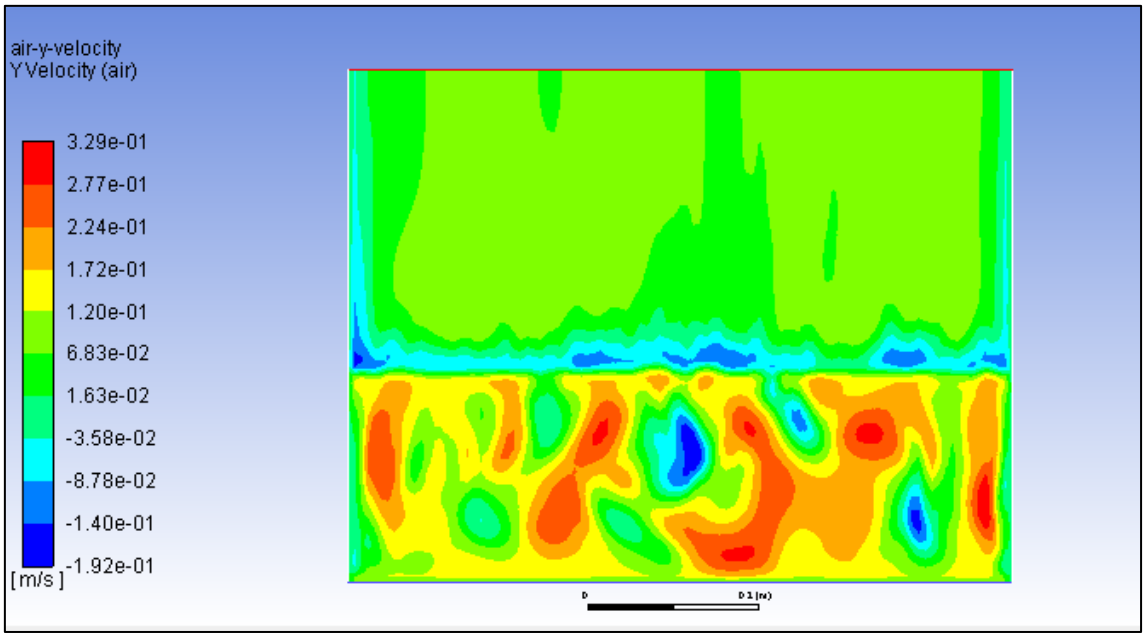

Figure 9.20. Air Y-velocity at 6s

- Solid Velocity

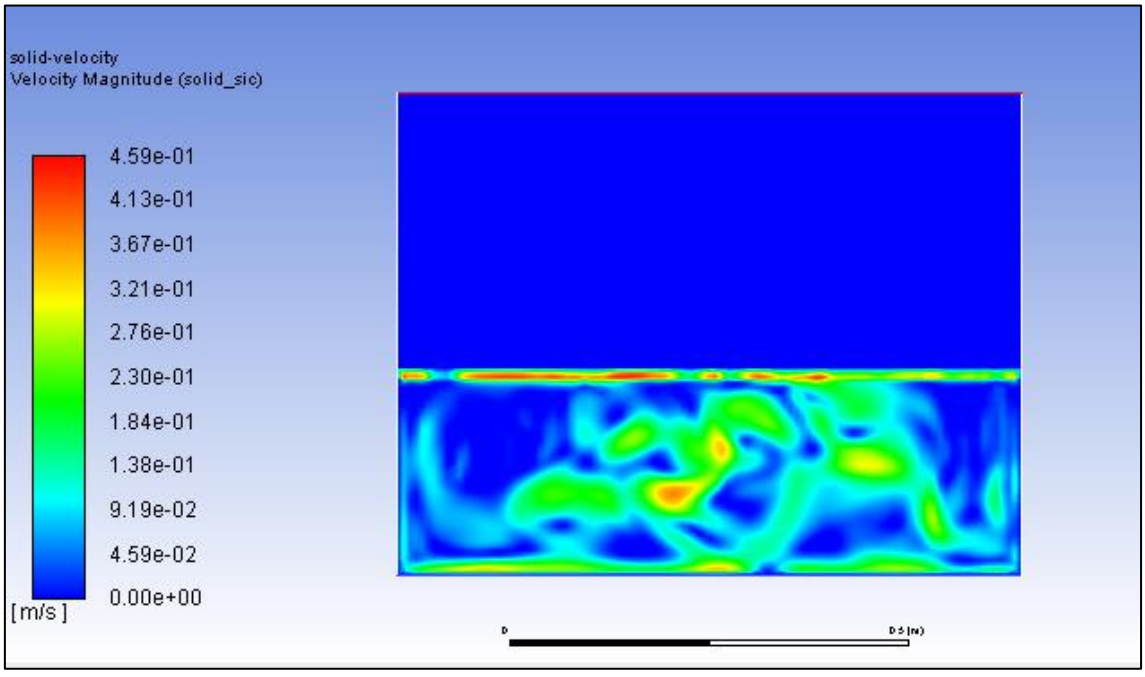

Figure 9.21. Solid velocity at 6s

- Solid Y-velocity

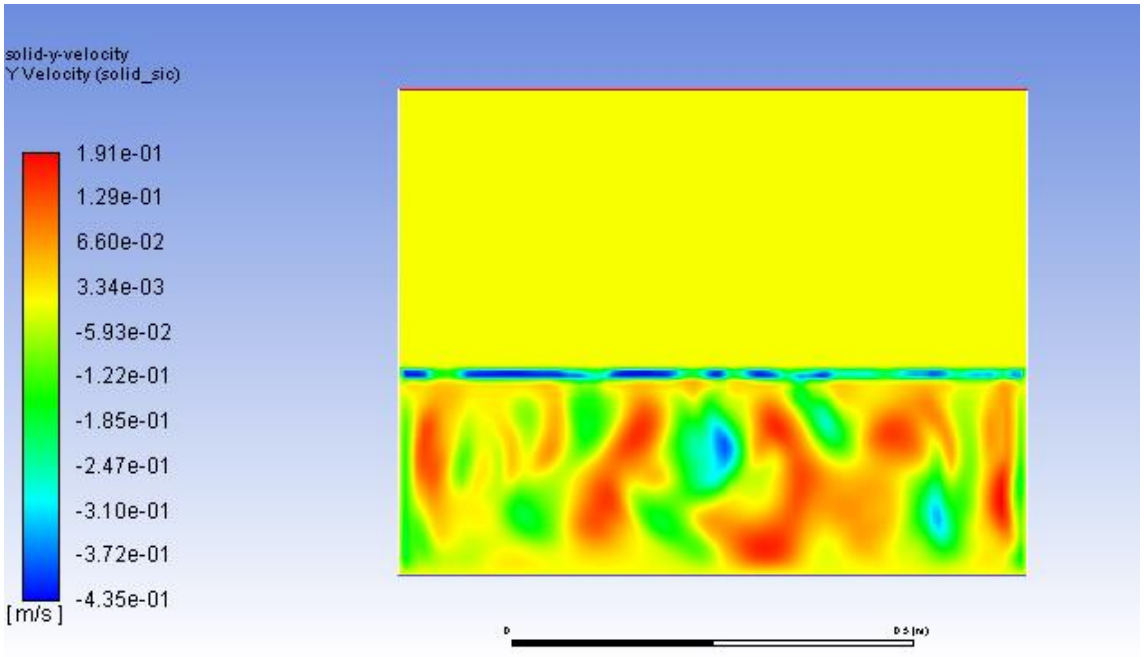

Figure 9.22. Solid Y-velocity at 6s

10 Heat source modeling

Once the cold fluidized bed model has been tested and check that it works properly, the next step is designing the model with heat transfer. The main challenges in this part of the study is define how can be the heat source modeled to match the experiment. First, it is important to know how does the heat source behavior. Then, it must be decided where exactly is the heat source going to be applied. Moreover, as it will be shown in this section, the size of the mesh and the intensity of the flux have a huge impact in the type of results obtained. So, the main objective is to create a heat source that has a similar behavior that the one shown in the experiment.

10.1 Heat Source

As it has been explained in *section 7.3.1*, the heat source of that experiment is a short-arc ozone-free 4 kW_{el} Xe lamp. That lamp was chosen to simulate the solar radiation as it has a very similar spectrum than the terrestrial solar radiation. For being able to implement that source in the Ansys model, the heat flux that this lamp produces is needed. The authors of the study [7], provide the spatial distribution of radiative heat flux incident on the bed surface. To characterize it they use a water cooled radiative heat flux sensor (Vatell TG-9000, calibration range: 0-1300 kW/m^2) to calculate the convective heat flux. The infrared camera was used to record the spatial distribution of the incident radiative flux. The flux measured by the radiative sensor was correlated with the fourth power of the bed temperature. That correlation was used to convert the temperature map into the heat flux spatial distribution reported in *Figure 10.1*.

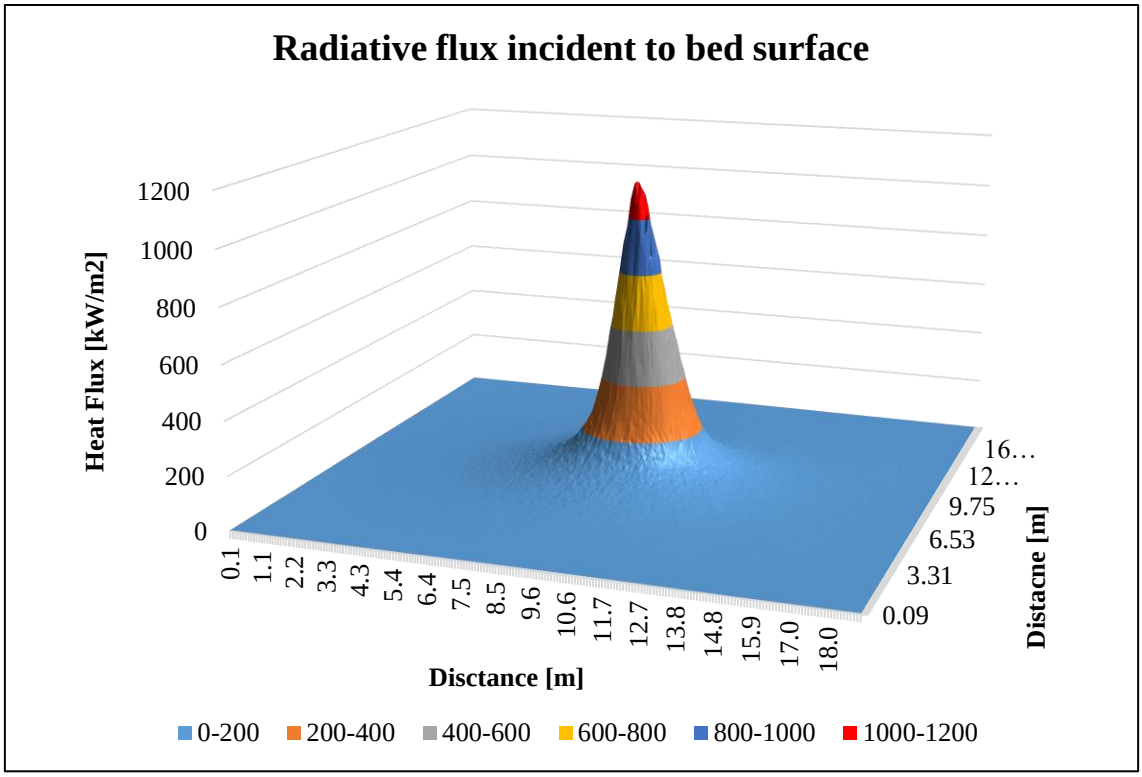

Figure 10.1. 3D representation of the radiative flux [kW/m^2] incident to bed surface

That 3-D representation was turned into a 2-D heat flux distribution to be implemented in the Ansys model. To create that 2-D version the previous representation was sliced in the point where the maximum heat flux was found. The heat source points the center of the bed and it can be observed that the major effect is concentrated less than 5 cm from the focal point. So, a very high gradient in the heat flux appears in a very small region.

As it can be observed in *Figure 10.3*, the shape of the incident flux is like a Gaussian distribution. So, the data has been fitted to a three, five and eight terms Gaussian distributions with a midpoint of 0.39 and a width of 0.78. The R^2 obtained with each one has been 0.9995, 0.9997, 0.9999. It has been considered adequate to choose the 3 terms Gaussian distribution to model the heat flux because it fits very well the data and is simpler than the other two candidates. In *Figure 10.2*, the Gaussian distribution can be observed and the data from the experiments. It can be appreciated that the fit of the distribution with the data is very good.

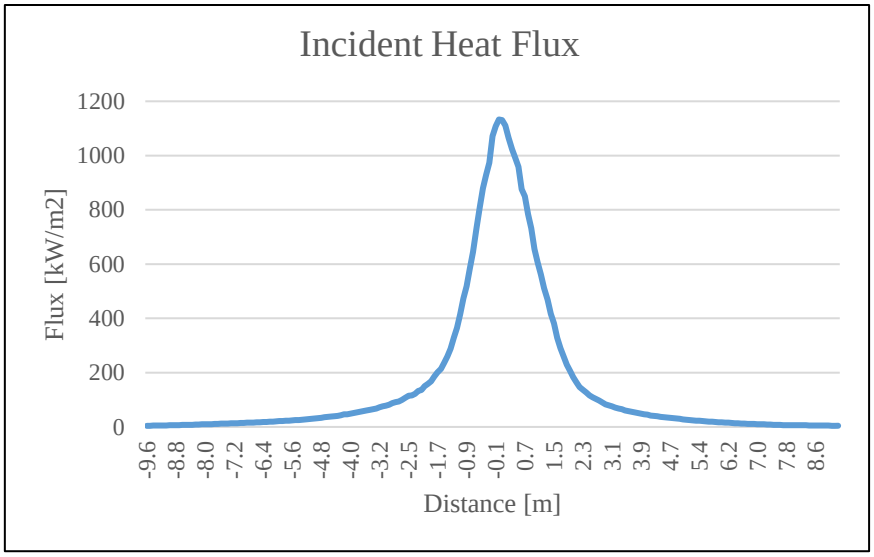

Figure 10.3. 2D representation of the radiative flux [kW/m^2] incident to bed surface

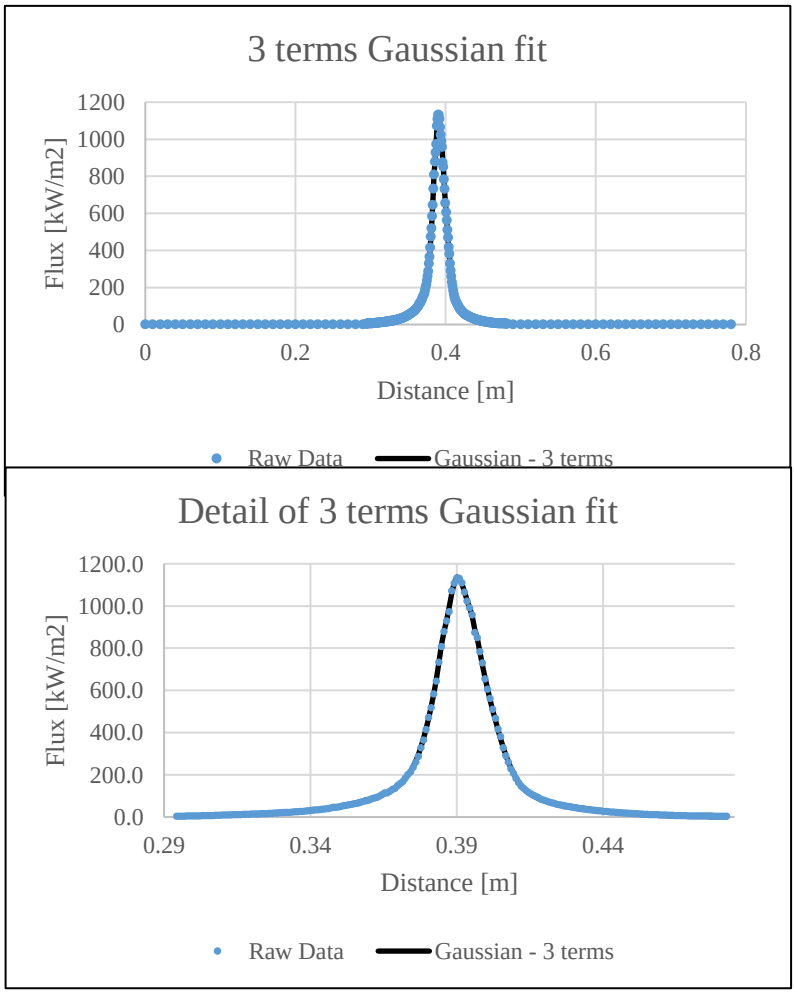

Figure 10.2. Gaussian distribution that fits of heat flux data (top); Detail of the Gaussian distribution ((bottom)

10.2 Application of heat source

Once the heat source term is defined that main question is how it is applied to the model. As the heat source must affect the surface of the bed, a way to track always the surface and apply the heat term to that cells must be designed. Other important issues that may arise are: how to take into consideration that the surface layer can have different solid volume fractions and the number of particles that contains each cell. If we have a very big cell, the number of particles in the cell will be high that if we have a more refined mesh. So, the effect of the mesh size will be studied to see its effect in the final result. Also, as we are heating up an entire cell, without considering the particles inside them, this will affect also to the conduction with the adjacent cells. The mesh size has a direct effect in the number of particles that receive that receive the radiation. Finally, the heat flux expression has been corrected to try to consider that the heat flux is affecting only the first layer. So, the corrected heat flux is the total flux divided by the size of the particle

11 Fixed bed simulation

The first case that has been simulated with the heat source has been the fixed bed. In that simulation, the is no injection of air so all the heat is absorbed by the solid particles of the bed. The mesh size has been set to fifty times the diameter of the solid particles, so the mesh size is 50*0.000127m = 0.00635m. The main objective of that case is analyzing the evolution of the temperature in the fixed bed surface and see if it matches with the experimental data.

Type of Solver	Pressure-Based
Solver Velocity Function	Absolute
Solver Time	Transient
Solver 2D Space	Planar
Gravity (m/s^2)	-9.81 (Y-direction)
Multiphase Model	Eulerian
Energy Model	ON
Viscous Model	Laminar
Properties of solid phase	
Density (kg/m^3)	3210
Specific Heat (J/kg·K)	690
Thermal Conductivity (W/m·K)	118
Diameter (m)	0.000127
Granular viscosity (kg/m·s)	syamlal-obrien
Granular Bulk Viscosity (kg/m·s)	lun-et-al
Frictional Viscosity (kg/m·s)	schaffer
Angle Of Internal Friction (deg)	30.0007
Frictional Pressure (Pa)	johnson-et-al
Frictional Modulus (Pa)	derived
Fraction Packing limit	0.5
Granular Conductivity (kg/m·s)	syamlal-obrien
Solid Pressure (Pa)	lun-et-al
Radial Distribution	lun-et-al
Elastic Modulus (Pa)	derived
Packing limit	0.64
Properties of wall material	
Density (kg/m^3)	8030
Specific Heat (J/kg·K)	502.48
Thermal Conductivity (W/m·K)	16.27
Phase Interaction	
Drag Coefficient	gidaspow
Heat Transfer Coefficient	gunn

Boundary Conditions	
Air Inlet velocity (m/s)	0
Solid Inlet velocity (m/s)	0
Granular Temperature (m^2/s^2)	0.0001
Volume Fraction	0
Temperature (K)	298
Gauge Pressure (Pa)	10000
Air Shear Condition	No slip
Solid Shear Condition	Specularity Coefficient = 0.7
Granular Conditions	Johnson-Jackson
Restitution Coefficient	0.9
Air Back Flow Temperature (K)	298
Solid Back Flow Temperature (K)	298

Table 11.1.Input data for the fixed bed case

11.1 Results of fixed bed case

In this section, the results obtained with the fixed bed case will be discussed and analyzed. The simulation was set to ten seconds to being able to compare the data obtained with the model with the data of the experiment. In *Figure 11.1*, it can be observed that the temperature in the focal point reaches very high temperatures very fast. In less than two seconds the temperature of the solid rises from 25ºC to more than 1500 ºC. Then, the temperature increases more slowly reaching a temperature around 2000 ºC at five seconds and 2250 ºC around 10s. The data reported on the experiment was that at 5 seconds the temperature was above 1500 ºC. As the measurement equipment used in the study is only able to measure temperatures up to 1500 ºC is very likely that the temperature of the focal point is very similar that the one calculated with the model.

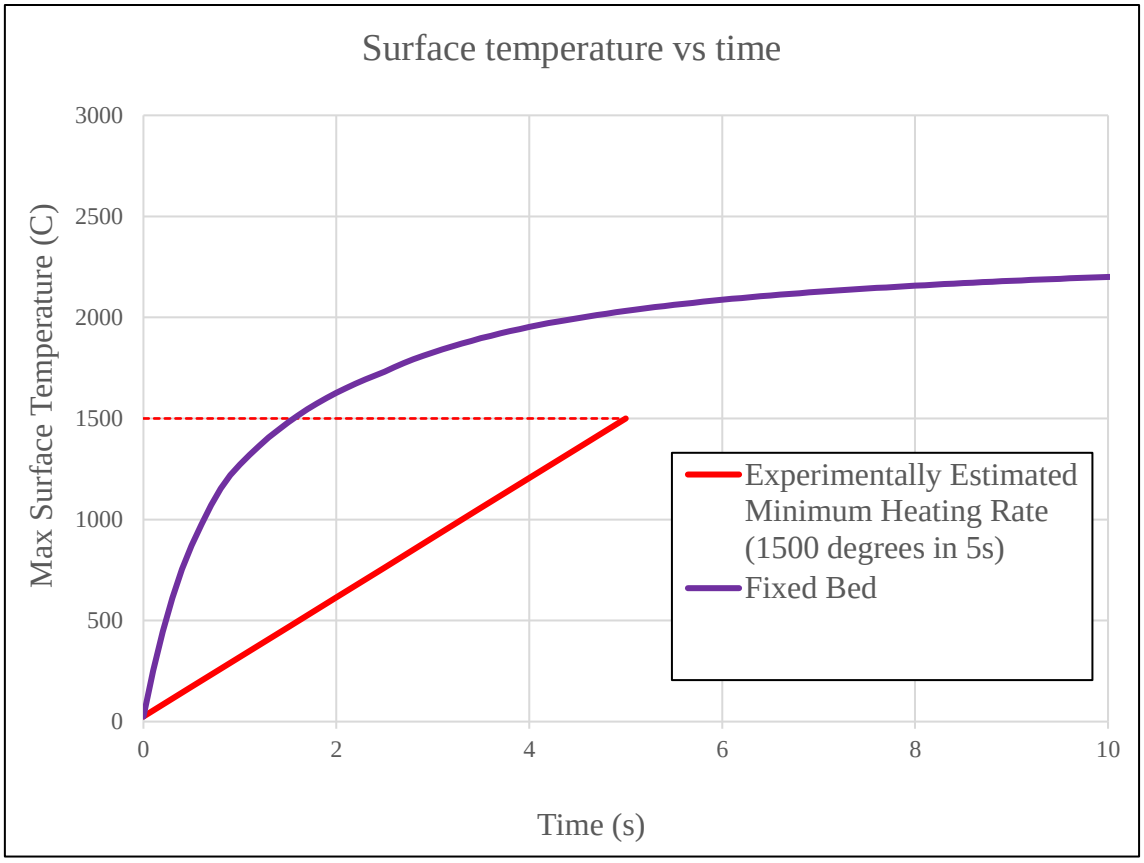

Figure 11.1. Evolution of temperature in the focal point vs time

In *Figure 11.2*, can be observed the temperature distribution of the fixed bed. The particles heat up around the focal point while the part of the bed is far from that point remains at a constant temperature. This type of behavior matches with the one reported in the paper. As it can be seen in *Figure 11.3*, the heat is transferred to the neighbor particles of the focal point. Although the view presented in the paper is the top view instead of the front view presented in the model the heat transfer between the particles matches.

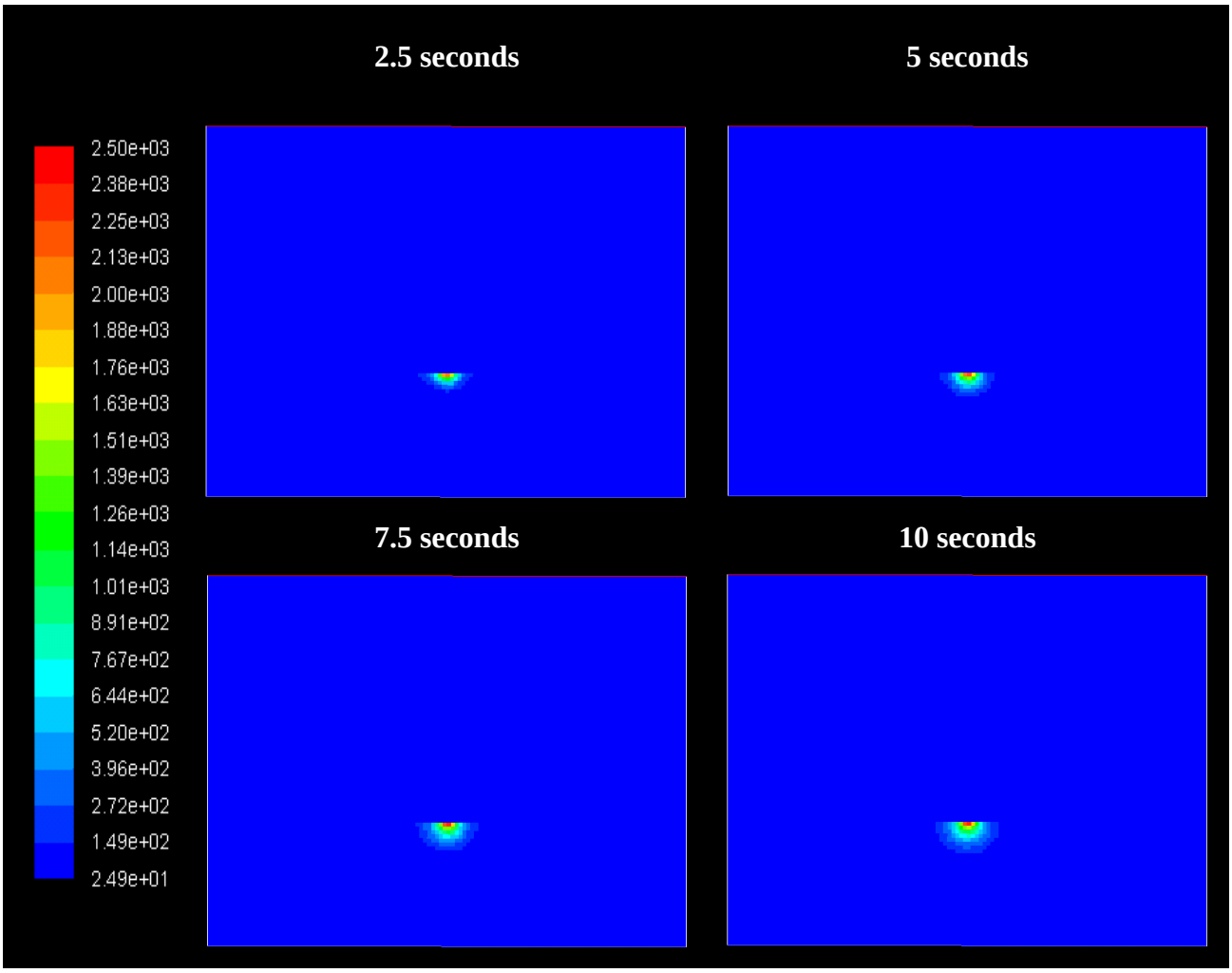

Figure 11.2. Temperature distribution in the fixed bed simulation for 2.5,5,7.5 & 10 seconds

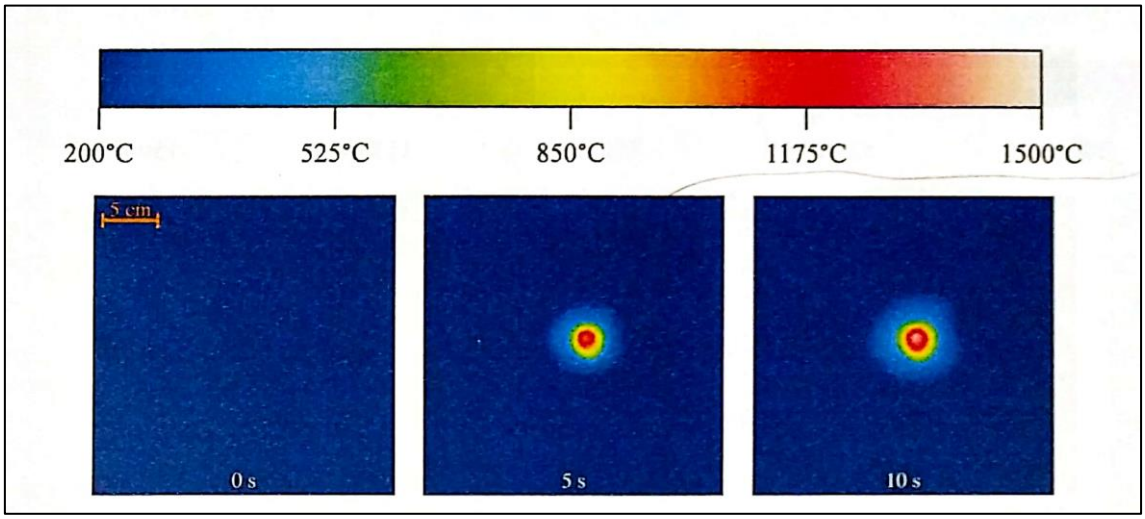

Figure 11.3. Temperature distribution of the surface of the bed view from above reported by the paper [7]

12 Fluidized bed simulation

In this section, the results obtained with the fluidized bed at four times the minimum fluidization velocity will be discussed and analyzed. The simulation was set to two seconds before the bed was already bubbling. So, once the fluidized bed was formed then the heat source term was activated.

Type of Solver	Pressure-Based
Solver Velocity Function	Absolute
Solver Time	Transient
Solver 2D Space	Planar
Gravity (m/s^2)	-9.81 (Y-direction)
Multiphase Model	Eulerian
Energy Model	ON
Viscous Model	Laminar
Properties of solid phase	
Density (kg/m^3)	3210
Specific Heat (J/kg·K)	690
Thermal Conductivity (W/m·K)	118
Diameter (m)	0.000127
Granular viscosity (kg/m·s)	syamlal-obrien
Granular Bulk Viscosity (kg/m·s)	lun-et-al
Frictional Viscosity (kg/m·s)	schaffer
Angle Of Internal Friction (deg)	30.0007
Frictional Pressure (Pa)	johnson-et-al
Frictional Modulus (Pa)	derived
Fraction Packing limit	0.5
Granular Conductivity (kg/m·s)	syamlal-obrien
Solid Pressure (Pa)	lun-et-al
Radial Distribution	lun-et-al
Elastic Modulus (Pa)	derived
Packing limit	0.64
Properties of wall material	
Density (kg/m^3)	8030
Specific Heat (J/kg·K)	502.48
Thermal Conductivity (W/m·K)	16.27
Phase Interaction	
Drag Coefficient	gidaspow
Heat Transfer Coefficient	gunn
Boundary Conditions	
Air Inlet velocity (m/s)	0.073
Solid Inlet velocity (m/s)	0

Granular Temperature (m^2/s^2)	0.0001
Volume Fraction	0
Temperature (K)	298
Gauge Pressure (Pa)	10000
Air Shear Condition	No slip
Solid Shear Condition	Specularity Coefficient = 0.7
Granular Conditions	Johnson-Jackson
Restitution Coefficient	0.9
Air Back Flow Temperature (K)	298
Solid Back Flow Temperature (K)	298

Table 12.1. Input data for the fluidized bed case

12.1 Results of bubbling bed case

In this section, the results obtained with the fluidized bed case will be discussed and analyzed. As it can be observed in *Figure 12.1*, the temperature at the focal point of the bed varies significantly during time reaching temperatures up to 900 ºC and going down to 250 ºC. Bubbling reduces local overheating of the bed surface due to two mechanisms. The first one is that bubbles promote coverage of the hot central region with the cold particles located in the surroundings. The second mechanism is due bubbles promotes ejection and displacement of hot particles towards the colder regions of the fluidized bed.

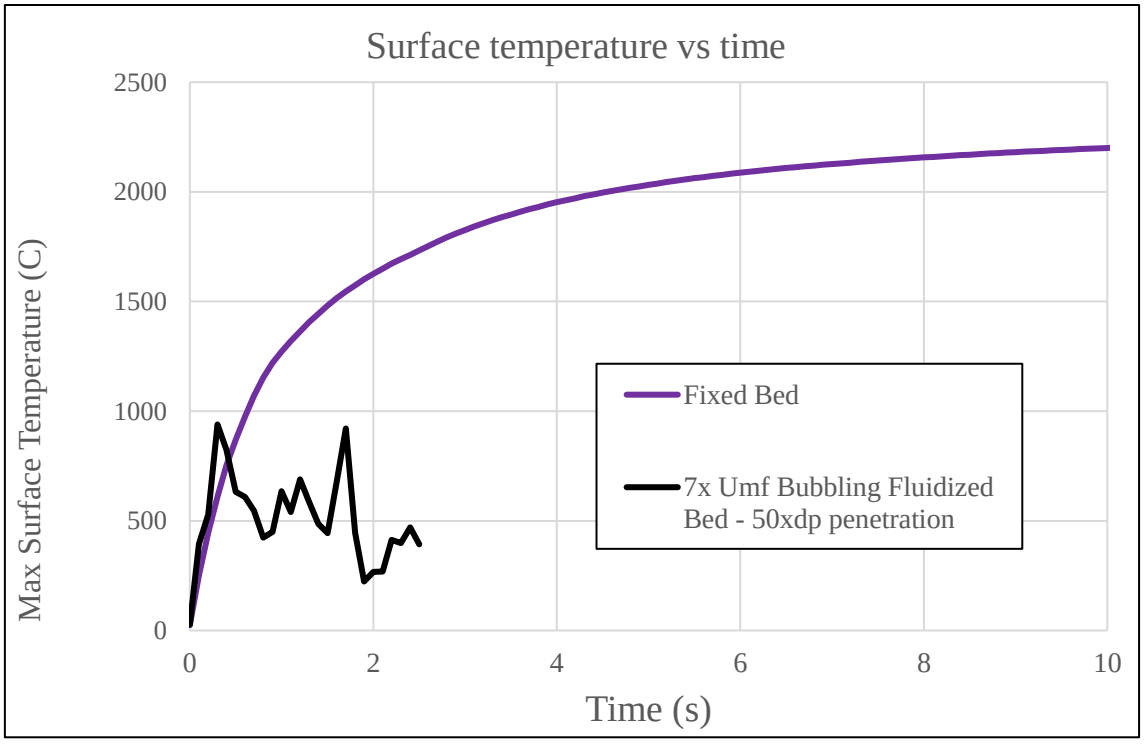

Figure 12.1. Evolution of temperature of the fluidized bed (black) and the fixed bed (purple) vs time

The solid volume fraction varies randomly during time. In Figure 12.2 can be observed the evolution of the volume fraction at 4 different times once the bed is already bubbling. The areas with a high solid volume fraction are marked in red and reaches values up to 0.57. In the blue areas, the concentration of particles is very low or null. It can be observed that inside the bed there are regions where the volume fraction is very low, in that regions is where the bubbles are located and are going to the surface to burst. This mixing increases the heat transfer and decreases the max temperature in the top of the bed.

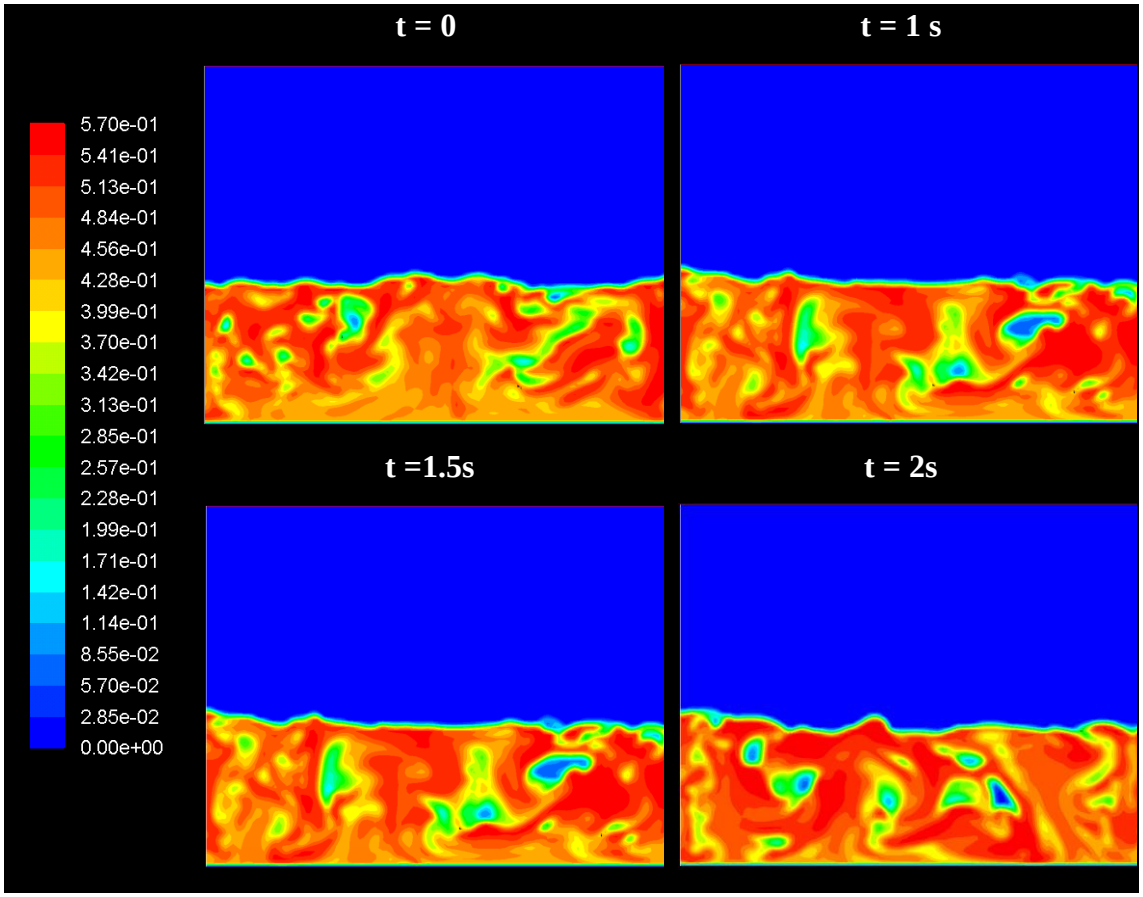

Figure 12.2. Solid volume fraction of the fluidized bed at 0,1,1.5 & 2 seconds

The temperature of solid particles depends on several factors but where the max temperature can be found is on the focal point of the heat source. As it can be observed in *Figure 12.3,* at 1 second the temperature in the focal point reaches a temperature of almost 1000K (727 ^{o}C) and then it decreases to 700K (427 ^{o}C) in less than a fraction of a second. So, it can be concluded that the temperature in the top part of the fluidized bed

will be constantly changing and while time advance a larger part of the bed will have been heated up.

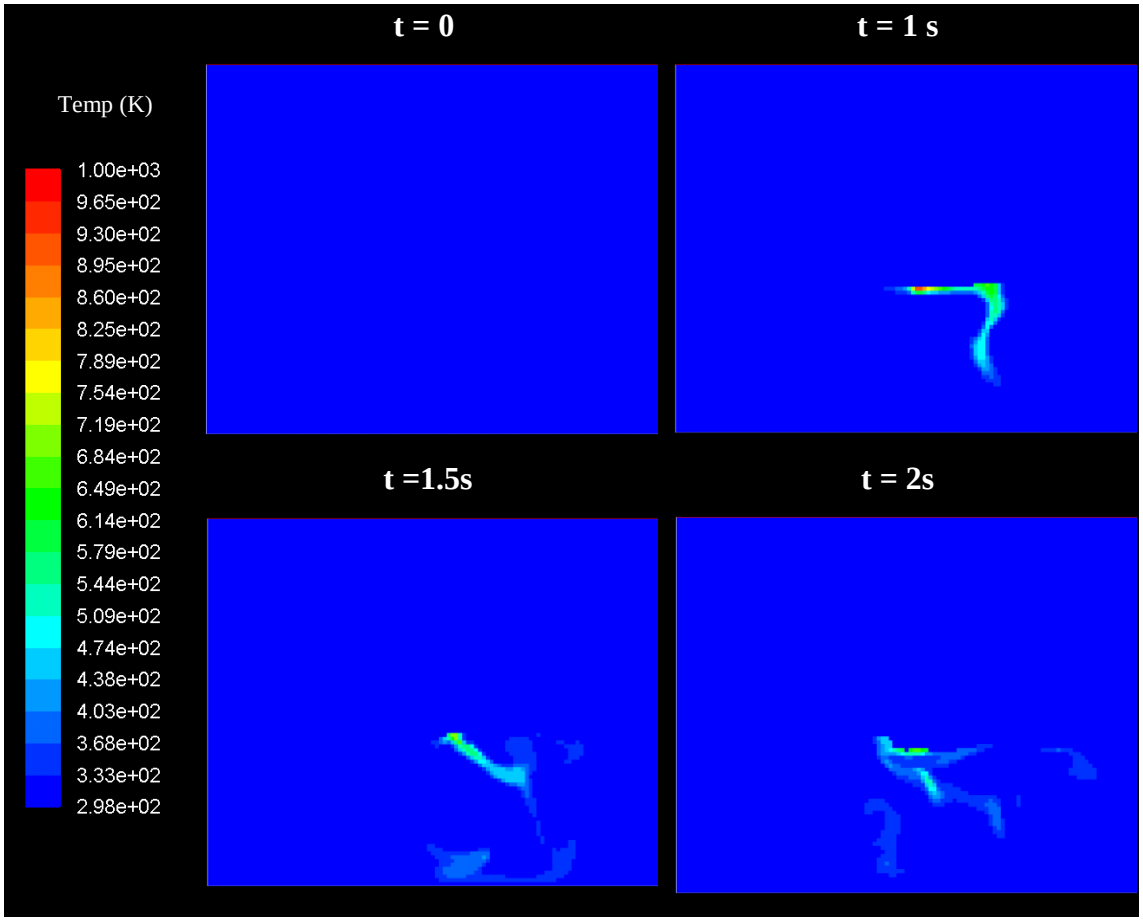

Figure 12.3. Solid temperature under bubbling conditions

Finally, another variable that it is interesting to study is the velocity of the solid particles. In *Figure 12. 4*, it can be observed that particles go up and down in the fluidized bed, creating vortex. It is also important to remark that the highest velocity appears on the bottom of the bed at the first seconds of the simulation. This gradient in velocity and mixing of the solid particles improves the heat transfer among the fluidized bed and decrease the maximum temperature reached in the focal point.

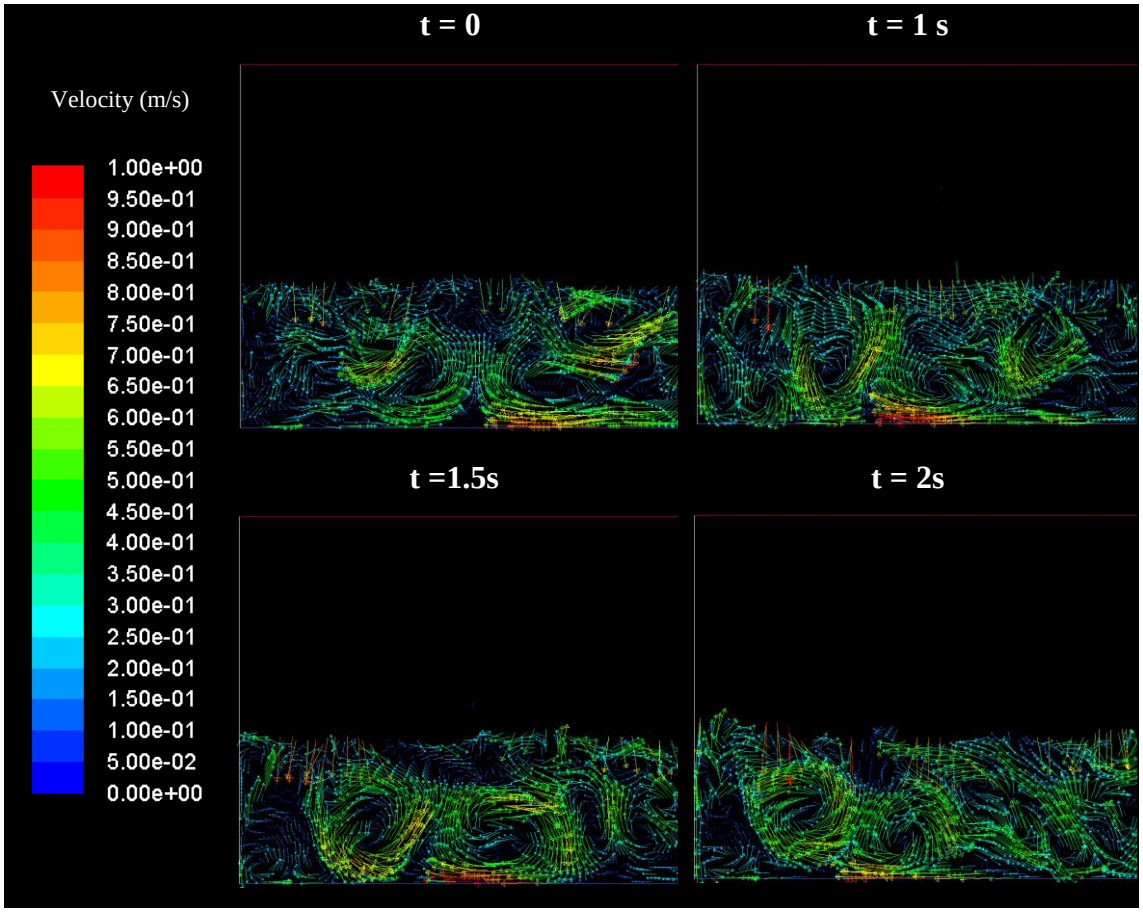

Figure 12. 4. Solid velocity under fluidized bed conditions

13 Conclusions

A CFD model being able to predict the behavior and understand the interactions in a fluidized bed when is irradiated with concentrated solar was developed. For the creation of the model it has been taken the study [7] as a base of the model and to be able to compare the results obtained.

A 2-D model of a rectangular fluidized bed with solid particles of SiC was developed. The models used for the drag coefficient and the heat exchange coefficient are Gidaspow and Gunn. These models were considered the best due to the characteristics of the simulation. The first simulation was tested without including the heat source and the results obtained were satisfactory, obtaining a fluidized bed when the air injection was four times the minimum fluidization velocity.

Then the model including the heat source was tested in two different cases. One of the main issues of that model was how to define the heat source that is affecting the fluidized bed. With the data obtained from the authors of the study, it was seen that the heat source fit a Gaussian distribution with a peak around 1200 kW/m^2 in the focal point. Then this heat source was introduced into the model affecting always the surface of the bed. The first case that was studied was the fix bed, so, with no injection of air. The temperature of focal point of the bed reaches a very high temperature, 2250 ^oC, in a very short span of time, in around 10s. This was due to a high amount of energy is concentered in a very small region. On the second case, the simulation was set with an injection velocity of four times the minimum fluidization velocity, which means that the bed was fully developed. The temperature of the bed, in the first two seconds of the simulation, varies along time from around 1000 ^oC to less than 300 ^oC. This is due to the face that now the bubbling bed make particles move chaotically increasing the interaction among them and improving the heat transfer in the bed. Bubbling reduces local overheating of the bed surface due to two mechanisms. The first one is that bubbles promote coverage of the hot central region with the cold particles located in the surroundings. The second mechanism is due bubbles promotes ejection and displacement of hot particles towards the colder regions of the fluidized bed.

Summarizing, a model able to predict the behavior of a fluidized bed when the heat source is radiating the top of the bed has been created and the results for the cases studied have been satisfactory.

14 Future work

Once the main cases have been analyzed and discussed some guidelines for continuing with the creation of the model will be provided. First, the results obtain vary significantly depending on the mesh size. This could be because the heat transfer model or the thermal conductivity of the model are not accurate. So, a deeper research in that fields should be done to perfect the model. The thermal conductivity may be improved if it includes the void fraction of each cell. On the other hand, the heat source term used in the simulation could diverge for the real experiment as a 2D version of it has been used. Moreover, the heat source data could also don't match the reality has it has been calculated experimentally. Summarizing, the heat transfer model, the thermal conductivity of the solid particles in the bed and the effect in the mesh size should be reviewed to perfect the heat model developed in that thesis.

15 References

[1] R. E. ADVISORS, 2016. [Online]. Available: http://www.renewable-energy-advisors.com/learn-more-2/levelized-cost-of-electricity/. [Accessed 28 December 2016].

[2] Fraunhofer, "Levelized cost of electricity renewable energy technologies," 2013.

[3] SOLGATE, "Solar Hybrid Gas Turbine Electric Power System," 2005.

[4] P. Heller, *Solar Energy*, no. 80, p. 1225, 2006.

[5] M. M. G. G. B. B. S. Z. Ma, "Development of a concentrating solar power system using fluidizedbed-bed technology for thermal energy conversion and solid particles for thermal energy storage," *Elseiver*, 2014.

[6] S. O. M. Bouhadda, "Modelling of heat transfer in a fluidized bed reactor irradiated indirectly by concentrated," *Elseiver*.

[7] R. C. Claudio Tregambi, "Heat transfer in directly irradiated fluidized beds," *ELSEIVER*, vol. 129, pp. 85-100, 2016.

[8] Y. K.Matsubara, "High-temperature fluidized receiver for concentratied solar radiation by a beam-down reflector system," *ELSEVIER*, vol. Energy Porcedia, no. 49, pp. 447-456, 2013.

[9] E. Abbasi, "Computational Fluid Dynamics and Population Balance Model for Simulation of Dry Sorbent CO2 Capture Process," Chicago, 2013.

[10] Ansys, "ANSYS Fluent Theory Guide," 2016.

[11] ASM, "ASM Aerospace Specification Metals Inc.," [Online]. Available: http://asm.matweb.com/search/SpecificMaterial.asp?bassnum=mq304a. [Accessed 12 May 2017].

[12] D. L. Q. Dr. Thomas Fend, "enerMEMA CSP Teaching Materias Chapter 1: Introduction," EnerMena.

[13] D. L. Q. Dr. Thomas Fend, "enerMENA Teaching Materials Chapter 2: Solar Radiation," ener MENA.

[14] B. O. D. N. Johanes Sattler, Asvanced CSP Teaching Materials, Chapter 8: Solar Tower Technology, enerMENA.

[15] begell, "Thermopedia," [Online]. Available: http://www.thermopedia.com/content/46/. [Accessed 23 January 2017].

[16] Kurimoto, "Continious Fluidized Bed," [Online]. Available: http://www.kurimoto.co.jp. [Accessed 30 April 2017].